Journal of Nanomaterials

Energy and Environmental Applications for 2D-Layered Nanomaterials

Lead Guest Editor: G. Ravi
Guest Editors: G. Ramalingam, Narayanan Subramanian, Baskaran Rangasamy, and Joice Sophia Ponraj

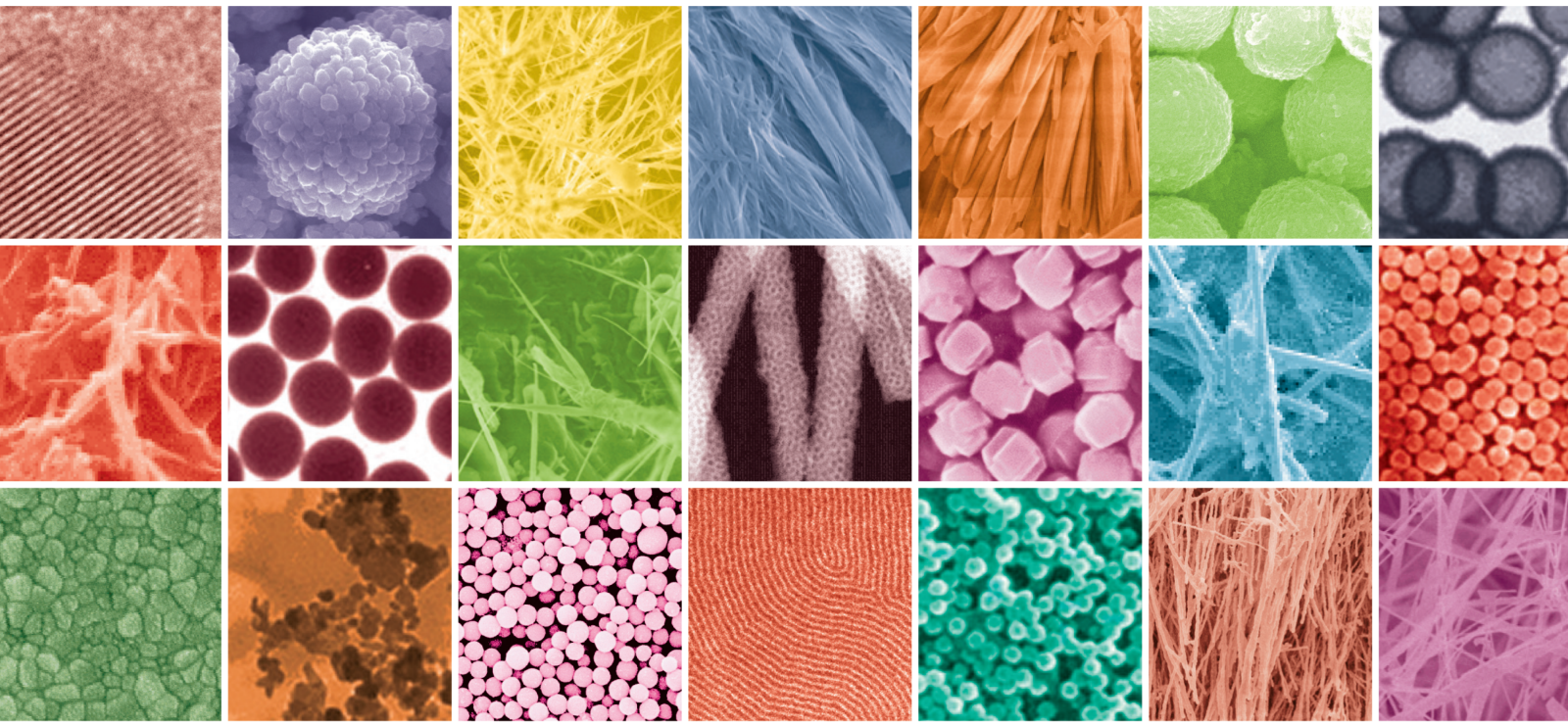

Energy and Environmental Applications for 2D-Layered Nanomaterials

Journal of Nanomaterials

Energy and Environmental Applications for 2D-Layered Nanomaterials

Lead Guest Editor: G. Ravi
Guest Editors: G. Ramalingam, Narayanan Subramanian, Baskaran Rangasamy, and Joice Sophia Ponraj

Contents

Hindawi
Journal of Nanomaterials
Volume 2021, Article ID 5533845, 8 pages
https://doi.org/10.1155/2021/5533845

Research Article

A Comparative Study of Nanostructures of CuO/Cu_2O Fabricated via Potentiostatic and Galvanostatic Anodization

S. Mary Margaret, Albin John P. Paul Winston, S. Muthupandi, P. Shobha, and P. Sagayaraj

Department of Physics, Loyola College (Autonomous), Chennai, Tamilnadu, India

Correspondence should be addressed to P. Sagayaraj; sagayaraj1962@gmail.com

Received 20 January 2021; Accepted 26 July 2021; Published 14 August 2021

Academic Editor: Joice Sophia Ponraj

A detailed comparative study on the synthesis process of coral-like CuO/Cu_2O nanorods (NRs) and nanopolycrystals (NPCs) fabricated on Cu foil employing aqueous electrolyte via potentiostatic (POT) and galvanostatic (GAL) modes is discussed. The structural, morphological, thermal, compositional, and molecular vibration of the prepared CuO/Cu_2O nanostructures was characterized by XRD, HRSEM, TG/DTA, FTIR, and EDX techniques. XRD analysis confirmed the crystalline phase of the formation of monoclinic CuO and cubic Cu_2O nanostructures with well-defined morphology. The average particle size was found to be 21.52 nm and 26.59 nm for NRs (POT) and NPCs (GAL), respectively, and this result is corroborated from the HRSEM analysis. POT synthesized nanoparticle depicted a higher thermal stability up to 600°C implying that the potentiostatically grown coral-like NRs exhibit a good crystallinity and well-ordered morphology.

1. Introduction

Development of efficient energy storage devices has gained a tremendous attention in recent years and. In this scenario, supercapacitors are emerging electrochemical energy storing devices due to its enormous properties like high power density, safe operational quality, fast charging/discharging rate, faster response time, long-term cycle stability and ecofriendliness [1–8]. Transition metal oxide/hydroxide such as CoO [9, 10], RuO_2 [11], NiO [12, 13], MgO, CuO [14–18], TiO_2 [19, 20], and FeO [21, 22] is the most commonly used electrode material in a electrochemical setup, and they determine the electrochemical performance of the supercapacitors [23]. Among these transition metal oxides, CuO is a multifunctional material, and it has versatile properties like inexpensiveness, low-toxicity, high theoretical capacity (670 $mAhg^{-1}$), and low electrical conductivity [24–26].

The two forms of Cu, namely, cuprous oxide (Cu_2O) that has a bandgap of ~2.17 eV and copper oxide (CuO) that has a bandgap of ~1.2–1.5 eV, are identified as excellent p-type semiconductors. Therefore, these materials can be used as electrodes in supercapacitors [27, 28], infrared photo detectors [29], lithium ion batteries [30], and photovoltaic solar cells [31]. Previous studies have been stimulated by these excellent properties to synthesizeCuO-Cu_2O nanoparticles [32]. It is evident from literature reviews that the bicomponent functional materials have improved the properties of super capacitors to greater extent than those of single component with morphologies such as CuO-Cu_2O nanowires [33], CuO-Cu_2O microspheres [34], nanorods [35, 36], CuO-Cu_2O nano-flowers [36], Leaf-Like CuO-Cu_2O [37], Cu_2O films [38], nanoribbons [39], Cu_2O nanocorals [40], and Cu_2O polycrystal [41]. The widely used processing routes among the various methods reported in the literature to fabricate CuO-Cu_2O are the hydrothermal method, electrochemical deposition [42], electrostatic spray deposition (ESD), sonochemical methods [43], and chemical bath method.

The one-step electrochemical deposition method is adopted for the fabrication of CuO/Cu_2O in the present work because

(i) It is a low-temperature growth process

(ii) Unbinding structure [44]

(iii) Constant temperature bath maintenance during phase composition

(iv) pH dependant

(v) Low applied potential to attain high degree of crystalline

(vi) High conductivity [45]

Although CuO/Cu_2O is abundant in nature, the most challenging issue is that they are highly unstable in aqueous phases. An attempt is therefore made in the present work to study the formation mechanism of CuO/Cu_2O nanostructures with various morphologies on Cu surface based on potentiostatic (POT) and galvanostatic(GAL) modes in NaOH, an aqueous electrolyte with pH ≥ 10 [46]. The comparative study fascinatingly helps to identify the prominent structures in which large amount of electrons could be packed into a small surface area that may help promoting the applications of the super capacitors.

2. Experimental Details

2.1. Materials. All the chemicals are of analytical grade and were used without further purification. High-purity copper foil (99.99%, 0.25 mm thick) was purchased from Sigma-Aldrich. NaOH from (Merck, India). Deionized water (DI) was obtained from the Deionizer Millipore Simplicity UV system, alumina powder has been procured from Merck, and acetone (99.5% purity), isopropyl alcohol (98% purity), and ethanol (96% purity) were purchased from Sigma-Aldrich. Hydrochloric acid (37%) was purchased from Emplura Merck. Pt mesh was bought from Sigma-Aldrich.

2.2. Synthesis of CuO/Cu_2O Coral-like Nanorods and Nanopolycrystals. Copper foil was uniformly cut into small pieces in the dimension of $2 \times 1\ cm^2$ and then polished with 0.2 μm alumina powder for the removal of the native oxide followed by a DI water rinse. Cu foils were ultrasonically cleaned in acetone, isopropyl alcohol, ethanol, and deionized water consecutively for 15 min and then immersed in 1.0 mold m^{-3} of HCL (35%) solution to remove surface impurities. The surface of the copper foil turned bright and smooth after the treatment. The precleaned Cu foils were then dried in air, and teflon tape was used to cover for one-sided anodization. In typical synthesis procedure, potentiostatic (POT) and galvanostatic (GAL) anodization was performed using two-electrode cell with Cu foil as the working electrode (WE). Pt mesh was used as a counter electrode (CE), and 1 M NaOH aqueous solution is used as electrolyte. Elico pH meter was used to confirm the alkaline nature (pH =12).

The working electrode and the counter electrode are placed at a constant distance of 3 cm to provide better dissemination of heat formed at the bottom of the pores. The distance between the WE and CE is maintained in order to attain a highly ordered pore diameter, wall thickness, and rod dimension. During the anodization process, a constant voltage of about 20 V and a constant current density of about 10 mA cm^{-2} were set to using Keithley 2400 as DC power source for both POT and GAL approaches, respectively. The anodization took place for 480 seconds at room temperature (~28°C). Once the anodization time is complete, the foil was cleaned with ethanol to obtain the exfoliated nanoparticles. Subsequently, the amorphous samples were then crystallized by annealing at 350°C for 1 hour. Finally, a black colored uniform film on the Cu foils is obtained which was taken for further characterizations.

2.3. Instrumentation. The structure, phase, and crystalline of the CuO/Cu_2O of POT and GAL were investigated by the X-ray diffraction system (Bruker XRD 3003 TT) using monochromatic nickel filtered CuK_α ($\lambda = 1.5406$ Å) radiation. The Fourier transform infrared (FT-IR) spectral analysis was carried out using a Perkin Elmer Spectrum Two. Scanning electron microscope (SEM Quanta 200 FEG) was employed for morphological study. The instrument is attached with an energy dispersive X-ray spectrometry (EDX) for performing crystalline information from the few nanometer depths of the material surface.

3. Results and Discussion

Figure 1 illustrates the one-step electrochemical anodization process of fabricating the CuO/Cu_2O on Cu electrode. Under the effect of POT and GAL, the copper substrate was made to oxidize and release Cu^{2+} and Cu^{+} ions into the NaOH solution respectivley, while OH^- in the solution captured the Cu^{2+} and Cu^{+} ions to form $Cu(OH)_2$ and CuOH nuclei with the following reactions [31],

$$Cu \xrightarrow{\text{anodization}} Cu_2{}^{+} + 2e^{-}, \quad (1)$$

$$Cu \xrightarrow{\text{anodization}} Cu^{+} + e^{-}. \quad (2)$$

During the process of anodization, the Cu surface on interaction with the OH^- ions that form the electrolyte under the influence of potential will change from the brown color to a faint blue color due to the formation copper II hydroxide. Cuprate ions in the form of the complex $Cu(OH)_2{}^{-4}$ were generated at the substrate–electrolyte interface, which creates nucleating sites on the copper substrate. Because of the negative charge on $Cu(OH)_2{}^{-4}$, it gets attracted rapidly toward the copper anode, where this combination precipitates the creation of the $Cu(OH)_2$ film on Cu at the anode. The obtained copper hydroxide film being crystalline is engineered to enhance the band gap or the phase formation by calcination in the presence of oxygen to yield a black precipitate indicating the presence of both CuO and Cu_2O [6, 45, 47].

$$Cu^{2+} + OH^{-} \longrightarrow Cu(OH)_2\{\text{anode}\}, \quad (3)$$

$$Cu^{+} + OH^{-} \longrightarrow Cu(OH), \quad (4)$$

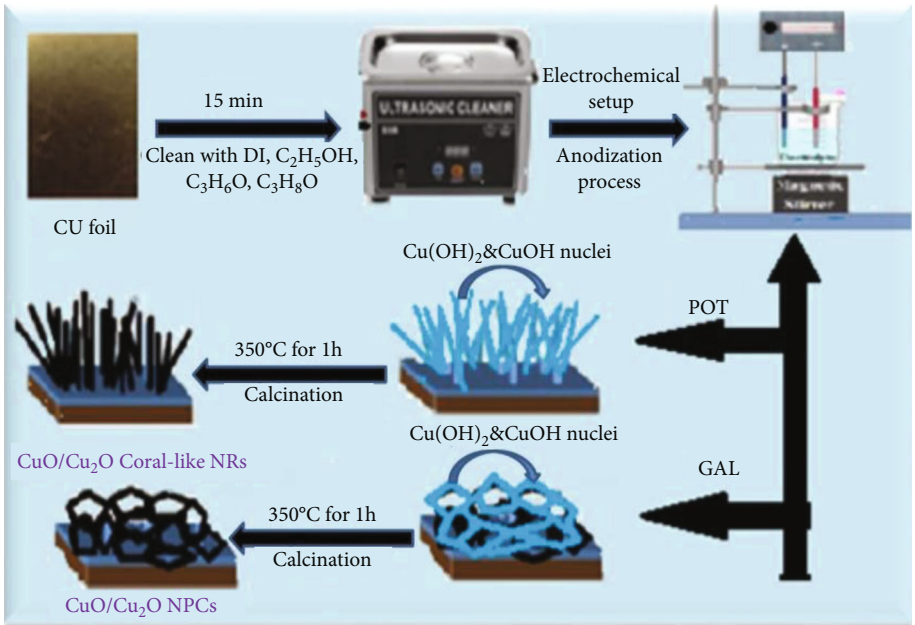

Figure 1: Schematic representation of fabrication of coral-like CuO/Cu_2O (NRs) and CuO/Cu_2O (NPCs) on Cu substrate.

$$Cu(OH)_2 \longrightarrow CuO + H_2O, \quad (5)$$

$$CuOH \longrightarrow Cu_2O + \frac{1}{2}H_2O. \quad (6)$$

XRD studies were carried out in order to understand the structural property of the prepared samples. The phase identification of a crystalline material and crystal structure of the *as*-prepared CuO-Cu_2O POT and GAL were analyzed by the XRD (Figure 2). The four peaks marked with diamond shape which can be indexed to the (111), (200), (111), and (-311) planes are presented in (Figure 2(a) and 2(b)) of the cubic Cu substrate (JCPDS No. 01-1241). The peaks are marked with clover shape which can be perfectly indexed to (002), (111), (-202), (202), (-311), and (220) planes of monoclinic CuO (JCPDS no. 89-2530), while the peaks marked with spade shape that can be indexed to the (111), (200), and (220) are the planes of the cubic Cu_2O (JCPDS no.77-0199), and no other crystalline peaks of impurities were observed which indicates that the *as*-prepared sample was highly pure. By using the Debye Scherrer formula, we could find average crystallite size (d) is calculated for both POT and GAL and was found to be ~21.52 nm and~26.59 nm, respectively. It is clearly evident that the sample obtained by the potentiostatic anodization (POT) shows small crystal size than that of the galvanostatic (GAL) method.

Figure 3 depicts the morphologies of nanostructures of CuO/Cu_2O investigated with scanning electron microscopy (SEM). Figures 3(a) and 3(b) exhibit coral-like CuO/Cu_2O nanorods (NRs) which are formed during the potentiostatic modes of anodization carried out at the rate of about 20 V, whereas (Figures 3(c) and 3(d)) represent high-magnification images of CuO/Cu_2O nanopolycrystals (NPCs) formed during galvanostatic modes of anodization

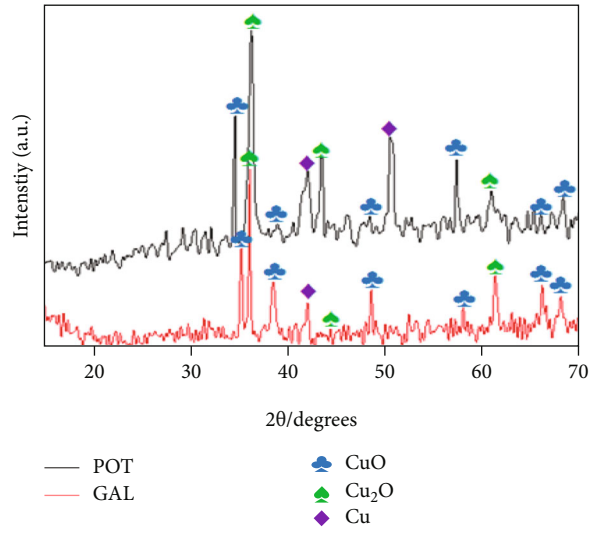

Figure 2: XRD pattern of the POT grown CuO/Cu_2O and GAL grown CuO/Cu_2O.

at the rate of about 10 mA cm^{-2}. The coral-like nanorods have a pointing tips that are around 26.9 nm and 29.3 nm presented in Figure 3(b) indicating a well-ordered morphology, demonstrating a controlled-size and rod-like structure which may help to enhance for the supercapacitor applications [48]. Figure 3(d) represents the size and shape of the CuO/Cu_2O nanopolycrystals (NPCs) that are around 50.3 nm and 57.2 nm which are in general larger in size compared to its counterpart.

The thermal stability of the nanomaterials was determined by thermogravimetry and differential thermal analysis (TG/DTA). The TG/DTA traces of CuO/Cu_2O nanoparticles are shown in (Figure 4). A small weight loss appears room temperature to 100°C recognized due to dehydration of

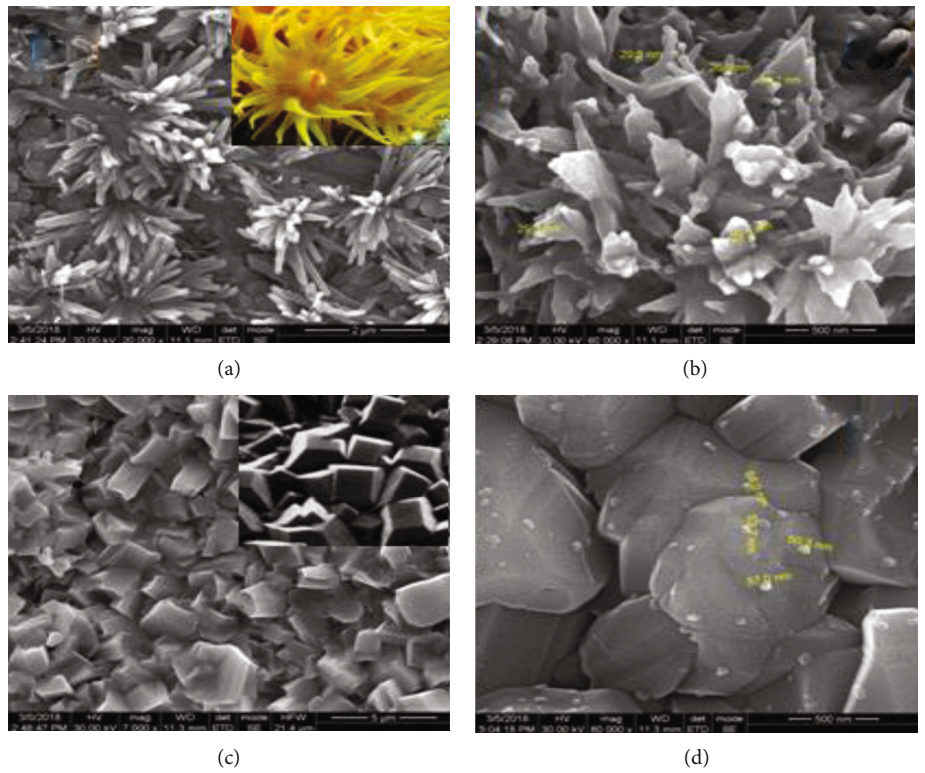

Figure 3: The high magnification SEM images of (a, b) POT grown CuO/Cu_2O (NRs) and (c, d) GAL grown CuO/Cu_2O (NPCs).

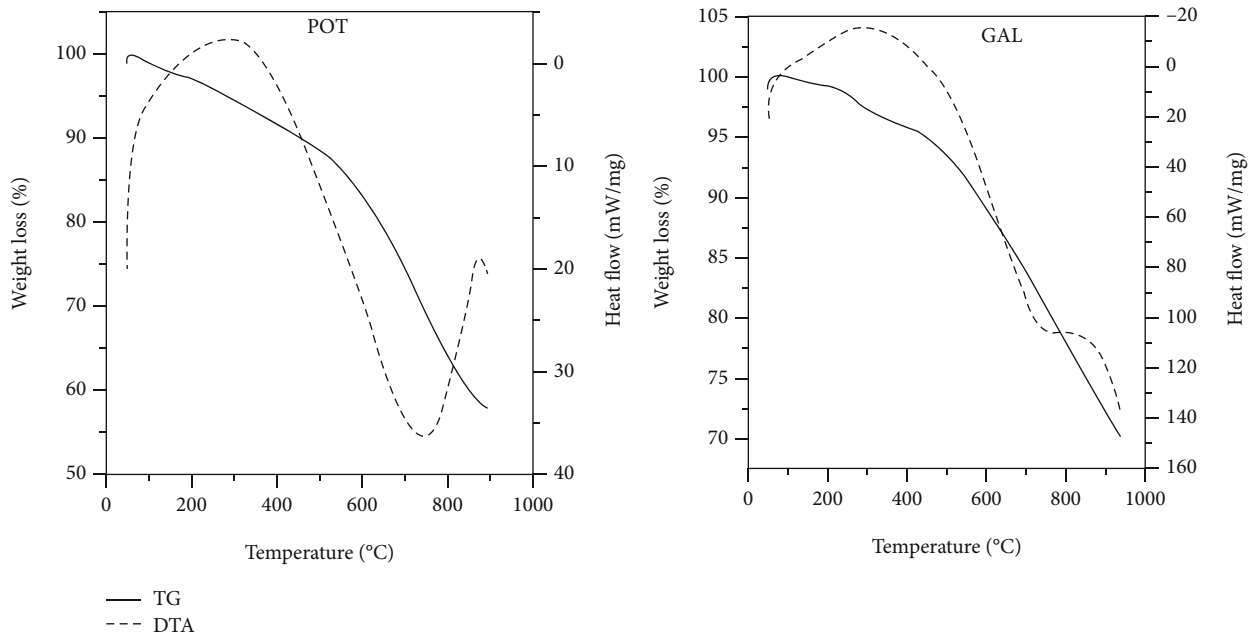

Figure 4: TG/DTA of CuO/Cu_2O for potentiostatic (POT) and galvanostatic (GAL) modes.

surface moisture. The POT samples gradually lose weight but is almost stable until 600°C with an estimated weight loss of 10%; on the other hand, GAL depicted a weight loss of 5% at 200°C and another 5% at 500°C and a slope nearing 20% at 600°C. From the TG graphs, it is clearly evident that the POT route synthesized samples were more stable at higher temperature than the GAL route.

FT-IR spectra of the CuO/Cu_2O nanostructures prepared in different modes are shown in (Figure 5). The broad absorption peaks at 3444 cm^{-1} and 3437 cm^{-1} belong to the

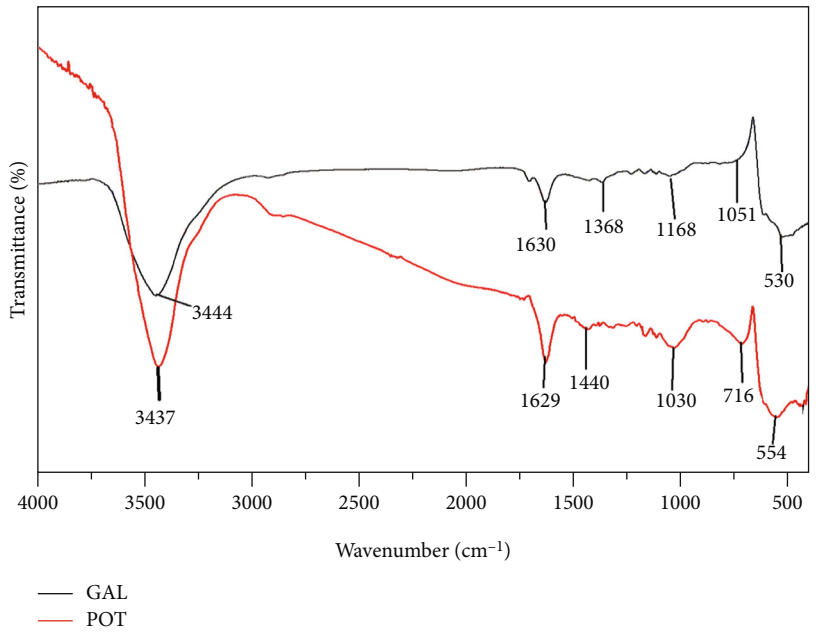

Figure 5: FT-IR spectra of CuO/Cu_2O NRs and NPCs prepared using different modes.

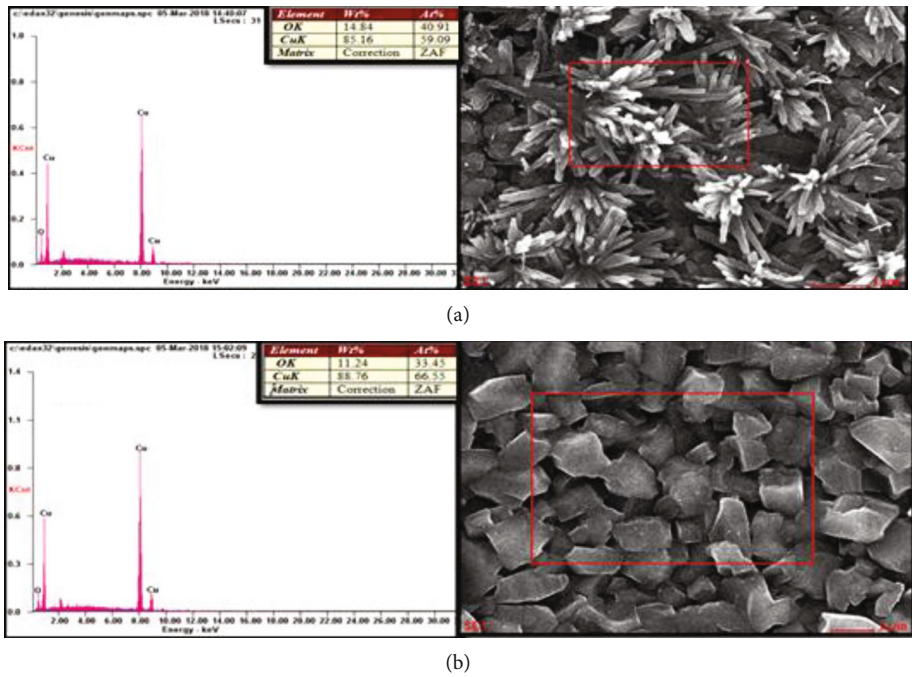

Figure 6: EDX spectra with SEM images of CuO/Cu_2O NRs and NPCs developed using different modes: (a) POT and (b) GAL.

symmetric or asymmetric stretching of O-H bonds. The peaks were observed at 1630 cm^{-1} and 1629 cm^{-1} indicate the formation of CuO nanoparticles. The stretching vibration of Cu-O bonds of Cu_2O nanoparticles is found at 1100-1400 $cm^{-1}$and shown in (Figure 5). The two infrared absorption peaks reveal the vibrational modes in the range of 500-700 cm^{-1}. The peaks observed at 530 cm^{-1} represent the formation of CuO/Cu_2O (NRs) and 554 cm^{-1} for $CuO/-Cu_2O$ (NPCs), respectively. Therefore, the metal-oxygen frequencies observed for CuO nanoparticles are in close agreement with those reported in the literature. Figure 6 shows the energy dispersive X-ray (EDX) analysis of POT (NRs) and GAL (NPCs) annealed at 350°C for 1 hr. Graphical representation reveals the presence of copper (Cu) and oxygen (O) elements in nanoparticals, and the data indicate that the nanocomposites are nearly stoichiometric. The weight percent of copper and oxide calculated from EDX analysis is shown in Figures 6(a) and 6(b). No other

Table 1: Comparison of research approaches and findings.

Substrate	Electrolyte	Time (min)	Morphology	Current/potential applied	References
Cu foil	2 M KOH	15	Nanowires	2.5 mA/cm^2	[49]
Cu foam	3 M KOH	20	Leaf-like	30 mA/cm^2	[37]
Cu foam	3 M KOH	30	Nanosheets	20 mA/cm^2	[50]
Cu foil	3 M KOH	120	Flower-like	6 mA/cm^2	[51]
Cu foil	0.1-0.5 M oxalate	30	Spheres	7.5-9 V	[52]
Cu foil	$Ni(NO_3)_2{\cdot}6H_2O$ (1 M)	5		1 mA/cm^2	[53]
Cu foil	2 M KOH	20	Needle	1.3 &1.8 V	[54]
	3 M KOH	20			
Cu foil	1 M NaOH	15	Rods	20 V (POT)	This work
	1 M NaOH	15	Particles	10 mA/cm^2 (GAL)	

elemental impurities are detected in the EDX spectra. This result confirmed that the formation of *as*-prepared metal oxides was CuO/Cu_2O nanoparticals. Table 1 describes a list of materials fabricated by a similar procedure.

4. Conclusion

In this paper, we have demonstrated a facile and cost-effective potentiostatic and galvanostatic modes of the anodization method to synthesize the coral-like CuO/Cu_2O nanorods and CuO/Cu_2O nanopolycrystals on copper foil. Fascinatingly, the comparative studies from the XRD patterns revealed that the galvanostatically anodized CuO/Cu_2O NPCs have a chaotic structure and large crystallite size on comparison with POT mode, whereas potentiostatically anodized coral-like NRs have a well-layered structure and binder less and smaller crystallite size as compared to the galvanostatic technique from HRSEM analysis. The thermal studies indicate that the POT mode fabricated samples were found to be more stable than the GAL mode. EDX analysis depicted a higher purity of both the samples.

Data Availability

The data supporting this work is available from the corresponding author upon request.

Conflicts of Interest

The authors declare that they have no conflicts of interest.

References

[1] P. Xu, J. Liu, T. Liu et al., "Preparation of binder-free CuO/Cu_2O/cu composites: a novel electrode material for supercapacitor applications," *RSC Advances*, vol. 6, no. 34, pp. 28270–28278, 2016.

[2] T. Zhu, S. Zheng, Y. Lu, Y. Chen, Y. Chen, and H. Guo, "Influence of iron concentration and post-annealing temperature on structure and pseudocapacitive characteristics of a MnO_2–Fe_2O_3 nanocomposite," *Journal of Solid State Electrochemistry*, vol. 19, no. 2, pp. 381–390, 2015.

[3] Q. Yu, H. Huang, R. Chen et al., "Synthesis of CuO nanowalnuts and nanoribbons from aqueous solution and their catalytic and electrochemical properties," *Nanoscale*, vol. 4, no. 8, pp. 2613–2620, 2012.

[4] X. Peng, J. Jin, Y. Nakamura, T. Ohno, and I. Ichinose, "Ultrafast permeation of water through protein-based membranes," *Nature Nanotechnology*, vol. 4, no. 6, pp. 353–357, 2009.

[5] H. Huang, Q. Yu, X. Peng, and Z. Ye, "Mesoporous protein thin films for molecule delivery," *Journal of Materials Chemistry*, vol. 21, no. 35, pp. 13172–13179, 2011.

[6] X. Peng, Q. Yu, Z. Ye, and I. Ichinose, "Flexible ultrathin free-standing fluorescent films of $CdSe_xS_1-$ x/ZnS nanocrystalline and protein," *Journal of Materials Chemistry*, vol. 21, no. 12, pp. 4424–4431, 2011.

[7] X. Peng, J. Jin, E. M. Ericsson, and I. Ichinose, "General method for ultrathin free-standing films of nanofibrous composite materials," *Journal of the American Chemical Society*, vol. 129, no. 27, pp. 8625–8633, 2007.

[8] J. Li, W. Cao, Y. Mao, Y. Ying, L. Sun, and X. Peng, "Zinc hydroxide nanostrands: unique precursors for synthesis of ZIF-8 thin membranes exhibiting high size-sieving ability for gas separation," *CrystEngComm*, vol. 16, no. 42, pp. 9788–9791, 2014.

[9] H.-P. Cong, X.-C. Ren, P. Wang, and S.-H. Yu, "Flexible graphene–polyaniline composite paper for high-performance supercapacitor," *Energy & Environmental Science*, vol. 6, no. 4, pp. 1185–1191, 2013.

[10] C. M. Magdalane, K. Kaviyarasu, M. V. Arularasu, K. Kanimozhi, and G. Ramalingam, "Structural and morphological properties of Co_3O_4 nanostructures: investigation of low temperature oxidation for photocatalytic application for waste water treatment," *Surfaces and Interfaces*, vol. 17, p. 100369, 2019.

[11] W. Wang, S. Guo, I. Lee et al., "Hydrous ruthenium oxide nanoparticles anchored to graphene and carbon nanotube hybrid foam for supercapacitors," *Scientific Reports*, vol. 4, no. 1, p. 4452, 2014.

[12] M. Wang, Y. Wang, H. Dou, G. Wei, and X. Wang, "Enhanced rate capability of nanostructured three-dimensional graphene/Ni_3S_2 composite for supercapacitor electrode," *Ceramics International*, vol. 42, no. 8, pp. 9858–9865, 2016.

[13] M. Huang, F. Li, Y. X. Zhang, B. Li, and X. Gao, "Hierarchical NiO nanoflake coated CuO flower core-shell nanostructures for supercapacitor," *Ceramics International*, vol. 40, no. 4, pp. 5533–5538, 2014.

[14] G. Wang, J. Huang, S. Chen, Y. Gao, and D. Cao, "Preparation and supercapacitance of CuO nanosheet arrays grown on nickel foam," *Journal of Power Sources*, vol. 196, no. 13, pp. 5756–5760, 2011.

[15] Y. Li, S. Chang, X. Liu et al., "Nanostructured CuO directly grown on copper foam and their supercapacitance performance," *Electrochimica Acta*, vol. 85, pp. 393–398, 2012.

[16] G. Ramalingam, R. Vignesh, C. Ragupathi, C. M. Magdalane, K. Kaviyarasu, and J. Kennedy, "Electrical and chemical stability of CuS nanofluids for conductivity of water soluble based nanocomposites," *Surfaces and Interfaces*, vol. 19, p. 100475, 2020.

[17] P. Surendran, A. Lakshmanan, S. Sakthy Priya et al., "Optical and nonlinear optical properties of $Zn_{0.96}Cu_{0.04}Al_2O_4$ nanocomposites prepared by combustion method," *Materials Today: Proceedings*, vol. 36, pp. 175–178, 2020.

[18] A. Lakshmanan, P. Surendran, S. SakthyPriya et al., "Effect of fuel content on nonlinear optical and antibacterial activities of $Zn/cu/Al_2O_4$ nanoparticles prepared by microwave-assisted combustion method," *J. King Saud Univ. - Sci.*, vol. 32, no. 2, pp. 1382–1389, 2020.

[19] B. Arjunkumar, G. Ramalingam, M. Ramesh, J. S. Ponraj, and K. V. Rao, "Investigation of uni-directional nanorods composed microspheres and branched TiO_2 nanorods towards solar cell application," *Materials Letters*, vol. 273, p. 127900, 2020.

[20] R. Gopal, M. M. Chinnapan, A. K. Bojarajan et al., "Facile synthesis and defect optimization of 2D-layered MoS_2 on TiO_2 heterostructure for industrial effluent, wastewater treatments," *Scientific Reports*, vol. 10, no. 1, p. 21625, 2020.

[21] F. Beshkar, H. Khojasteh, and M. Salavati-Niasari, "Recyclable magnetic superhydrophobic straw soot sponge for highly efficient oil/water separation," *Journal of Colloid and Interface Science*, vol. 497, pp. 57–65, 2017.

[22] S. Mortazavi-Derazkola, M. Salavati-Niasari, O. Amiri, and A. Abbasi, "Fabrication and characterization of Fe_3O_4@-SiO_2@TiO_2@Ho nanostructures as a novel and highly efficient photocatalyst for degradation of organic pollution," *Journal of Energy Chemistry*, vol. 26, no. 1, pp. 17–23, 2017.

[23] J. Huang, H. Wu, D. Cao, and G. Wang, "Influence of Ag doped CuO nanosheet arrays on electrochemical behaviors for supercapacitors," *Electrochimica Acta*, vol. 75, pp. 208–212, 2012.

[24] M. Zhi, C. Xiang, J. Li, M. Li, and N. Wu, "Nanostructured carbon–metal oxide composite electrodes for supercapacitors: a review," *Nanoscale*, vol. 5, no. 1, pp. 72–88, 2013.

[25] W. Zhang, M. Li, Q. Wang et al., "Hierarchical Self-assembly of Microscale Cog-like Superstructures for Enhanced Performance in Lithium-Ion Batteries," *Advanced Functional Materials*, vol. 21, no. 18, pp. 3516–3523, 2011.

[26] D. P. Volanti, M. O. Orlandi, J. Andrés, and E. Longo, "Efficient microwave-assisted hydrothermal synthesis of CuO sea urchin-like architectures via a mesoscale self-assembly," *CrystEngComm*, vol. 12, no. 6, pp. 1696–1699, 2010.

[27] X. Wang, C. Hu, H. Liu, G. Du, X. He, and Y. Xi, "Synthesis of CuO nanostructures and their application for nonenzymatic glucose sensing," *Sensors and Actuators B: Chemical*, vol. 144, no. 1, pp. 220–225, 2010.

[28] H. Chen, J.-H. Lee, Y.-H. Kim et al., "Metallic copper nanostructures synthesized by a facile hydrothermal method," *Journal of Nanoscience and Nanotechnology*, vol. 10, no. 1, pp. 629–636, 2010.

[29] M. Veerapandian, S. Sadhasivam, J. Choi, and K. Yun, "Glucosamine functionalized copper nanoparticles: preparation, characterization and enhancement of anti-bacterial activity by ultraviolet irradiation," *Chemical Engineering Journal*, vol. 209, pp. 558–567, 2012.

[30] S. Gao, S. Yang, J. Shu, S. Zhang, Z. Li, and K. Jiang, "Green fabrication of hierarchical CuO hollow micro/nanostructures and enhanced performance as electrode materials for lithium-ion batteries," *Journal of Physical Chemistry C*, vol. 112, no. 49, pp. 19324–19328, 2008.

[31] K. Krishnamoorthy and S.-J. Kim, "Growth, characterization and electrochemical properties of hierarchical CuO nanostructures for supercapacitor applications," *Materials Research Bulletin*, vol. 48, no. 9, pp. 3136–3139, 2013.

[32] B. Y. Xia, P. Yang, Y. Sun et al., "One-Dimensional Nanostructures: Synthesis, Characterization, and Applications," *Advanced Materials*, vol. 15, no. 5, pp. 353–389, 2003.

[33] L. Wang, W. Cheng, H. Gong et al., "Facile synthesis of nanocrystalline-assembled bundle-like CuO nanostructure with high rate capacities and enhanced cycling stability as an anode material for lithium-ion batteries," *Journal of Materials Chemistry*, vol. 22, no. 22, pp. 11297–11302, 2012.

[34] Y. Cheng, Y. Lin, J. Xu et al., "Surface plasmon resonance enhanced visible-light-driven photocatalytic activity in cu nanoparticles covered Cu_2O microspheres for degrading organic pollutants," *Applied Surface Science*, vol. 366, pp. 120–128, 2016.

[35] V. Scuderi, G. Amiard, S. Boninelli et al., "Photocatalytic activity of CuO and Cu_2O nanowires," *Materials Science in Semiconductor Processing*, vol. 42, pp. 89–93, 2016.

[36] Y. Luo, S. Li, Q. Ren et al., "Facile synthesis of flowerlike Cu2O nanoarchitectures by a solution phase route," *Crystal Growth & Design*, vol. 7, no. 1, pp. 87–92, 2007.

[37] D. He, G. Wang, G. Liu, H. Suo, and C. Zhao, "Construction of leaf-like CuO–Cu_2O nanocomposites on copper foam for high-performance supercapacitors," *Dalton Transactions*, vol. 46, no. 10, pp. 3318–3324, 2017.

[38] Y. Yang, Y. Li, and M. Pritzker, "Control of Cu_2O film morphology using potentiostatic pulsed electrodeposition," *Electrochimica Acta*, vol. 213, pp. 225–235, 2016.

[39] X. Wen, W. Zhang, S. Yang, Z. R. Dai, and Z. L. Wang, "Solution phase synthesis of Cu(OH)2Nanoribbons by coordination self-assembly using Cu2S nanowires as precursors," *Nano Letters*, vol. 2, no. 12, pp. 1397–1401, 2002.

[40] C.-H. Tsai, P.-H. Fei, and C.-H. Chen, "Investigation of coral-like Cu2O nano/microstructures as counter electrodes for dye-sensitized solar cells," *Materials (Basel).*, vol. 8, no. 9, pp. 5715–5729, 2015.

[41] A. Paracchino, J. C. Brauer, J.-E. Moser, E. Thimsen, and M. Graetzel, "Synthesis and characterization of high-photoactivity electrodeposited Cu2O solar absorber by photoelectrochemistry and ultrafast spectroscopy," *Journal of Physical Chemistry C*, vol. 116, no. 13, pp. 7341–7350, 2012.

[42] Y. Tan, X. Xue, Q. Peng, H. Zhao, T. Wang, and Y. Li, "Controllable fabrication and electrical performance of single crystalline Cu2O nanowires with high aspect ratios," *Nano Letters*, vol. 7, no. 12, pp. 3723–3728, 2007.

[43] R. V. Kumar, Y. Mastai, Y. Diamant, and A. Gedanken, "Sonochemical synthesis of amorphous cu and nanocrystalline

Cu2O embedded in a polyaniline matrix," *Journal of Materials Chemistry*, vol. 11, no. 4, pp. 1209–1213, 2001.

[44] N. G. Elfadill, M. R. Hashim, K. M. Chahrour, and S. A. Mohammed, "Electrochemical deposition of Na-doped p-type Cu_2O film on n-type Si for photovoltaic application," *Journal of Electroanalytical Chemistry*, vol. 767, pp. 7–12, 2016.

[45] A. Osherov, C. Zhu, and M. J. Panzer, "Influence of ITO electrode surface composition on the growth and optoelectronic properties of electrodeposited Cu2O thin films," *Journal of Physical Chemistry C*, vol. 117, no. 47, pp. 24937–24942, 2013.

[46] N. K. Allam and C. A. Grimes, "Formation of vertically oriented TiO2 nanotube arrays using a fluoride free HCl aqueous electrolyte," *Journal of Physical Chemistry C*, vol. 111, no. 35, pp. 13028–13032, 2007.

[47] R. S. Hyam, J. Lee, E. Cho, J. Khim, and H. Lee, "Synthesis of copper hydroxide and oxide nanostructures via anodization technique for efficient photocatalytic application," *Journal of Nanoscience and Nanotechnology*, vol. 12, no. 11, pp. 8396–8400, 2012.

[48] S. Zhao, T. Liu, Y. Zhang et al., "Cr-doped MnO_2 nanostructure: morphology evolution and electrochemical properties," *Journal of Materials Science: Materials in Electronics*, vol. 27, no. 4, pp. 3265–3270, 2016.

[49] J. Zhao, X. Shu, Y. Wang et al., "Construction of CuO/Cu_2@-CoO core shell nanowire arrays for high-performance supercapacitors," *Surface and Coatings Technology*, vol. 299, pp. 15–21, 2016.

[50] J. Bai, L. Yang, B. Dai et al., "Synthesis of CuO-Cu_2@graphene nanosheet arrays with accurate hybrid nanostructures and tunable electrochemical properties," *Applied Surface Science*, vol. 452, pp. 259–267, 2018.

[51] P. V. Dat and N. X. Viet, "Facile synthesis of novel areca flower like Cu_2O nanowire on copper foil for a highly sensitive enzyme-free glucose sensor," *Materials Science and Engineering: C*, vol. 103, p. 109758, 2019.

[52] M. H. Mahmood, Suryanto, M. H. F. al Hazza, and F. I. Haider, "Influence of Oxalate Concentration and Temperature on the Microstructure Morphology of Nano Anodized Copper Coating," *Journal of Materials Science and Engineering A*, vol. 8, no. 4, pp. 155–165, 2018.

[53] X. Shu, Y. Wang, Y. Qin et al., "Synthesis and supercapacitive performance of CuO/Cu_2O nanosheet arrays modified by hydrothermal deposited NiOOH," *Journal of Solid State Electrochemistry*, vol. 21, no. 5, pp. 1489–1497, 2017.

[54] L. C. T. Shoute, K. M. Alam, E. Vahidzadeh et al., "Effect of morphology on the photoelectrochemical performance of nanostructured Cu_2O photocathodes," *Nanotechnology*, vol. 32, no. 37, p. 374001, 2021.

Hindawi
Journal of Nanomaterials
Volume 2021, Article ID 5540219, 12 pages
https://doi.org/10.1155/2021/5540219

Research Article

Performance of Natural Dye Extracted from Annatto, Black Plum, Turmeric, Red Spinach, and Cactus as Photosensitizers in TiO_2NP/TiNT Composites for Solar Cell Applications

Shibu Joseph,[1] Albin John P. Paul Winston,[2] S. Muthupandi,[2] P. Shobha,[2] S. Mary Margaret,[2] and P. Sagayaraj[2]

[1]*Department of Physics, St. Xavier's College, Thiruvananthapuram 695586, India*
[2]*Department of Physics, Loyola College (Autonomous), Chennai 600034, India*

Correspondence should be addressed to P. Sagayaraj; sagayaraj1962@gmail.com

Received 11 February 2021; Revised 10 June 2021; Accepted 25 July 2021; Published 10 August 2021

Academic Editor: Narayanan Subramanian

This paper is aimed at how to select, extract, and characterize natural dyes and to use them as sensitizers in dye-sensitized solar cells (DSSCs). Dyes obtained from fresh sources of annatto fruits, black plums, cactus fruits, turmeric roots, and red spinach leaves were used as sensitizers. The dye pigments were analyzed using UV-Vis spectrophotometer and FT-IR for the characterization of their spectral properties. The combination from Titanium dioxide paste with the powdered nanotubes was used as photoanodes for DSSCs. The photovoltaic properties of the DSSCs such as efficiency, fill factor, open-circuit voltage, and short circuit current were studied using a standard illumination of air-mass 1.5 global (AM 1.5 G) having an irradiance of 100 mW/cm^2. The highest power conversion efficiencies (η) of 0.7% was achieved for the DSSCs fabricated using dye extracted from annatto fruits and 0.4% each for dyes extracted from black plum fruits and cactus fruits, respectively. The widespread accessibility of these fruits, roots, and leaves and ease of extraction of dyes from these ordinarily available natural resources render them unique and low-cost candidates for solar cell fabrication.

1. Introduction

The emergence of dye-sensitized solar cells (DSSCs) was pioneered by O'Regan and Grätzel in 1991 [1]. The dye as a sensitizer in a DSSC plays a key role in absorbing sunlight and transforming solar energy into electric energy. DSSCs belong to the third generation in the photovoltaic devices, and they also hold a good relation for the low-cost conversion of solar energy to electricity due to the rather simpler materials and lower cost of fabrication [2]. The essential need for the innovative selection of materials for the photosensitizing applications led to the production and improvement in DSSCs [3–5]. These cells are based on the coating of the glass with a suitable nanostructured, mesoporous metal oxide films anchored to the visible light with the aid of adsorbed molecular dye. The injection of the electrons forms the excited states of the dye to the conduction band of the metal oxides. The passing electrons travel along the current-carrying collector, while the dye gets regenerated by the electron donor within the electrolyte solution. Usually, the dyes are generated from plant leaves, fruits, and other naturally occurring products. Several papers have been reported in this regard [6–16]. Although metal complex-based DSSCs have provided a relatively high efficiency, their limited resources and costly production remain to be a major disadvantage. Recently, organic dyes with related characteristics that of Ru-based compound having higher absorption coefficients have been reported [17–20]. Organic dyes used in the DSSC often show similarity to natural dyes that are found in plant leaves, fruits, and other natural products. Employing natural dyes as sensitizers DSSC is emerging as a prevalent area of research due to their low cost, nontoxicity, and far-reaching biodegradation. Thus far, numerous natural dyes have been employed as sensitizers in DSSC [21–26]. In the recent past,

(a) Annatto seeds (b) Black plum fruits

(c) Turmeric roots (d) Red spinach leave

(e) Cactus fruits (f) The extracted dyes

Figure 1: Photographs of selected natural products for dye extraction.

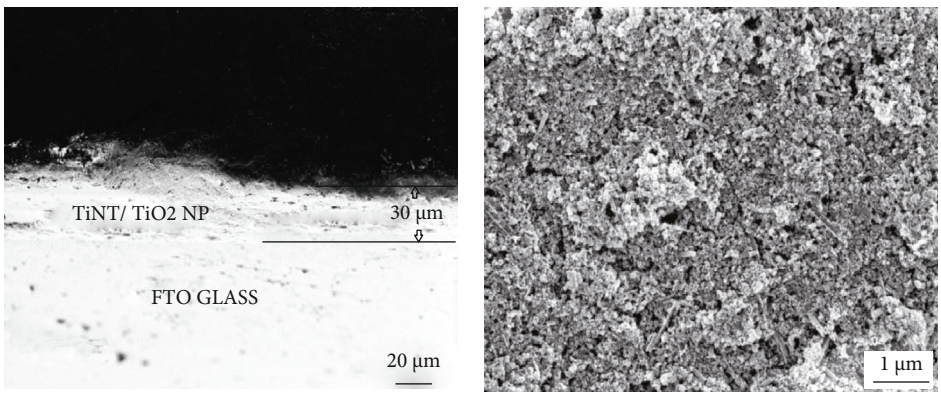

(a) Vertical view (~30 μm) (b) Top view

Figure 2: FESEM images of TiNT/TiO_2 NP on FTO glass.

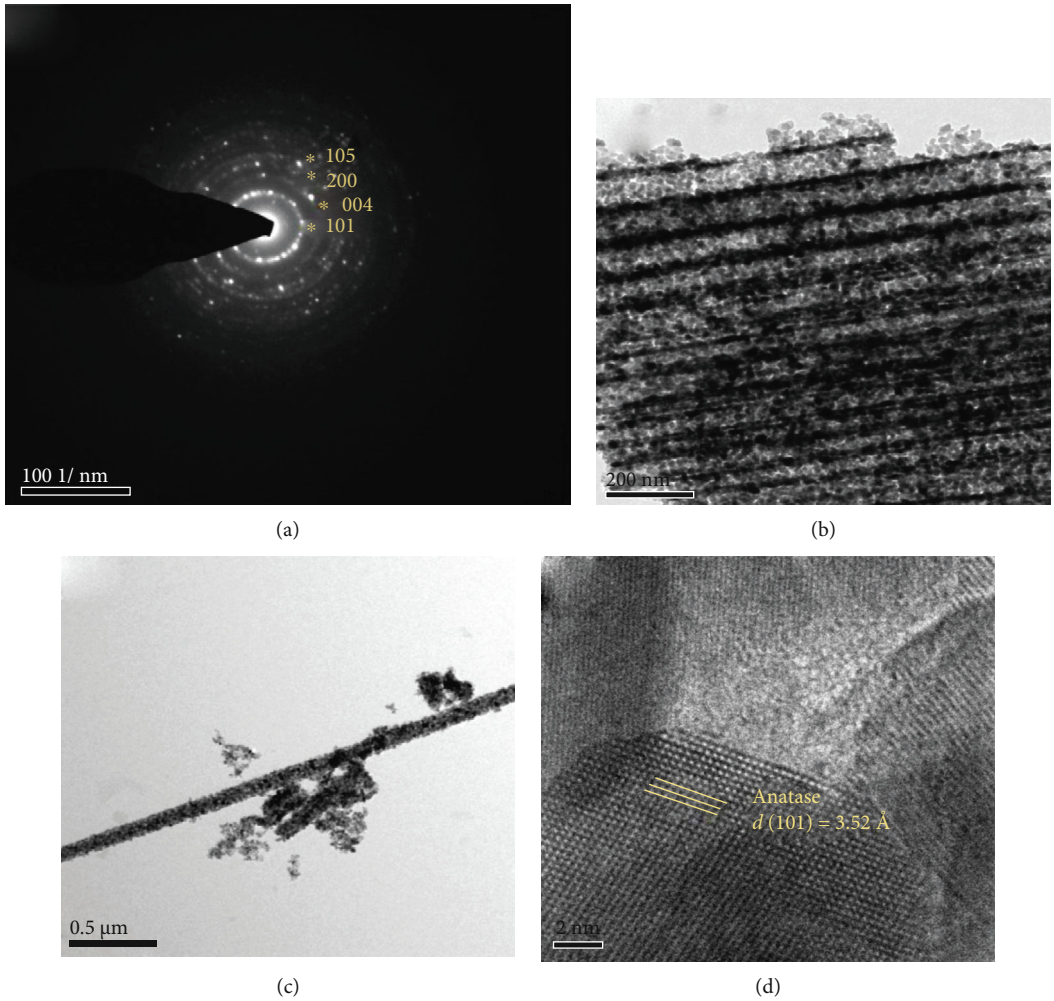

Figure 3: HRTEM images of the synthesized TiNT: (a) the SAED pattern showing the crystal lattices, (b and c) the nanotube bundle, and (d) the crystal lattice.

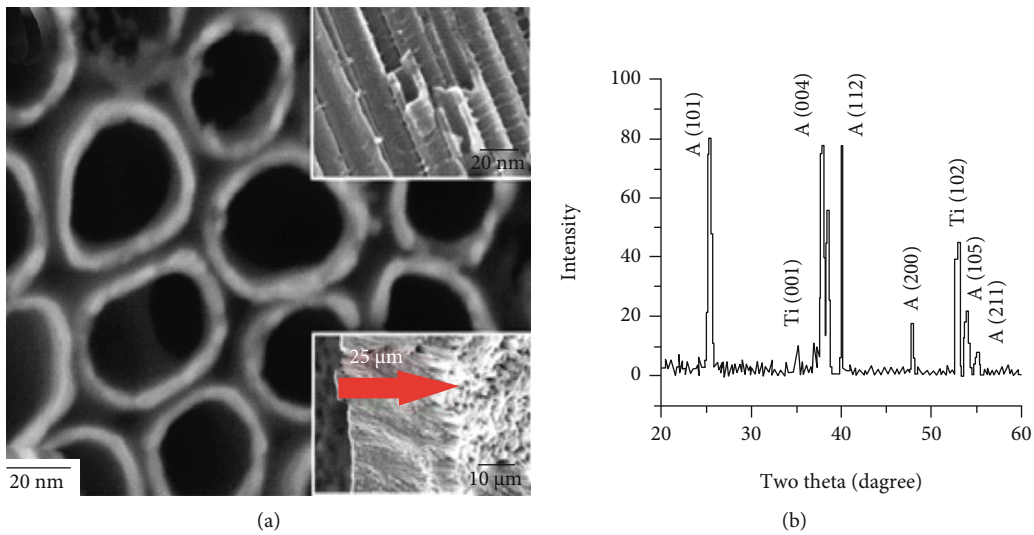

Figure 4: (a) The FESEM image of the TiO_2NT and (b) the XRD pattern of the TiO_2NT.

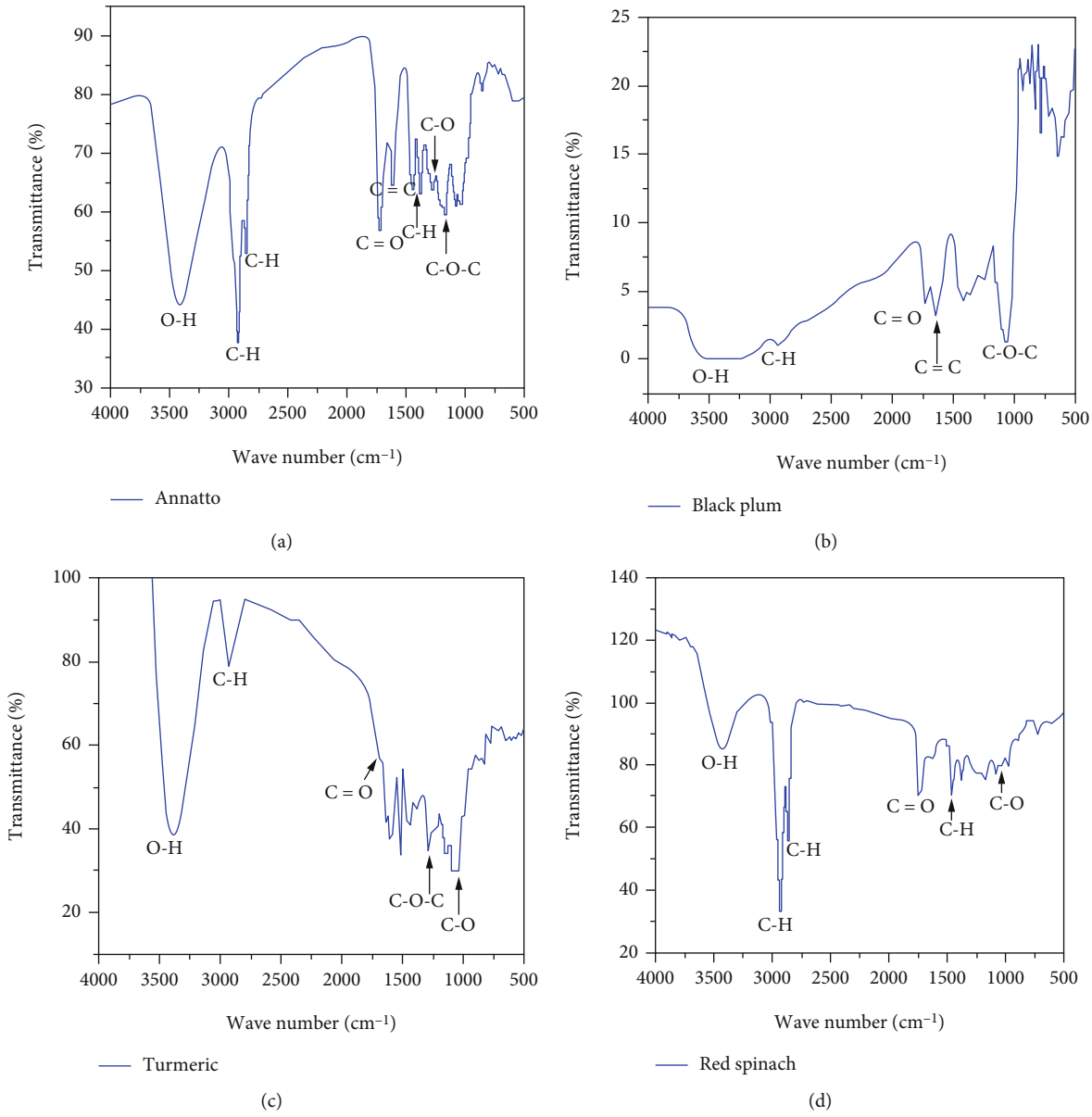

Figure 5: Continued.

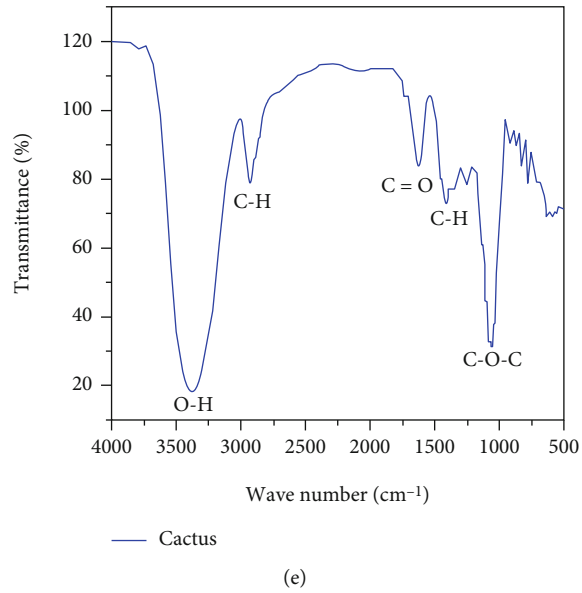

Figure 5: FT-IR spectra of (a) annatto dye, (b) black plum dye, (c) turmeric dye, (d) red spinach dye, and (e) cactus dye.

several steps have been taken to optimize the structure of these natural dyes to improve the efficiency of DSSC, and the outcomes are promising.

This paper summarizes the work of five different types of natural dyes extracted from various fruits, leaves, and roots which are found common in the southern part of India. UV-Vis absorption and FT-IR spectroscopy studies were carried out on the extracted dyes. The photovoltaic properties of natural DSSCs were also investigated.

2. Material and Methods

2.1. Preparation of TiO_2 Nanotubes. TiO_2 nanotubes were synthesized by the anodization method where ethylene glycol (EG) electrolyte is used in the presence of NH_4F. Ti foils (0.5 mm thickness, 99.4% purity, Sigma Aldrich) were successively cleaned before anodization in acetone, ethanol, and deionized (DI) water. Anodization was performed in a two-electrode arrangement with titanium foil as the cathode and platinum foil as the anode [25–27]. Keithley 2400 was used as the voltage source to drive the anodization. The electrolyte consisted of 0.3 wt% NH_4F and 2 vol% H_2O in ethylene glycol. The anodization was conducted at 60 V for 12 h at room temperature. After the prescribed duration, the anodized samples were annealed at 450°C for 2 h in air. The annealed samples were characterized using FESEM and EDAX to study the surface morphology and chemical composition of the synthesized materials. XRD and HRTEM analyses were carried out to evaluate the crystalline nature of the samples. Later, the annealed freestanding tube arrays were crushed into powder and mixed well with the TiO_2 NP paste (Dysol Ltd.) to form the photoanode. The detailed preparation method is illustrated in our previous article [28].

2.2. Preparation of Natural Dye Sensitizers. The annatto seeds were collected from fresh fruits and vacuum dried at 60°C. After drying, these seeds were dipped in absolute ethanol at room temperature in the dark for 24 h, and then, the solution was filtered to remove the seeds and other solid particles. The filtered solution was then used as sensitizer. The dye attained from black plums is as follows; fresh fruits were collected and the black skins of the fruits were carefully separated and dried in vacuum. After drying, the product was immersed in ethanol for 24 h to extract the dye. The solids were then filtered out from the dye solution. Similarly, fresh cactus fruits were collected, washed, and crushed well in ethanol solution and kept for 24 h to extract the dye. Once the ethanol solution became deep red in color, the solids were removed from the solution by filtration.

To obtain turmeric dye, fresh turmeric roots were cut into small pieces and dipped in ethanol for 24 h and filtered out to obtain dark yellow turmeric dye. The dye from red spinach leaves was extracted with acetone. The leaves were dried sufficiently well in a dark room. The dried leaves were crushed and soaked in acetone for 24 h, and a fine green colored dye was obtained. The red color disappeared once the leaves got dried.

Figure 1 demonstrates the five different natural dyes which were used as the sensitizers. These natural dyes were used to sensitize the photoanodes prepared from the composite of TiO_2 nanoparticle/TiO_2 nanotube paste (TiO_2 NP/TiNT). Later, DSSCs were assembled, and the photoelectrical properties were inspected.

2.3. Fabrication of Natural Dye-Sensitized Solar Cells. The natural dye-sensitized solar cell (n-DSSC) was fabricated using TiO_2 NP/TiNT composite photoanodes with platinum sputtered FTO (Dyesol Ltd.) as counter electrode. The commercially available iodine/triiodide electrolyte (Dyesol Ltd.) was used as electrolyte solution in the preparation of n-DSSC. The sintered photoanodes after cooling into the normal temperature was immersed in to the solution containing natural dye for 24 h. Once the dye was completely absorbed by the photoanodes, it was sandwiched with the platinum

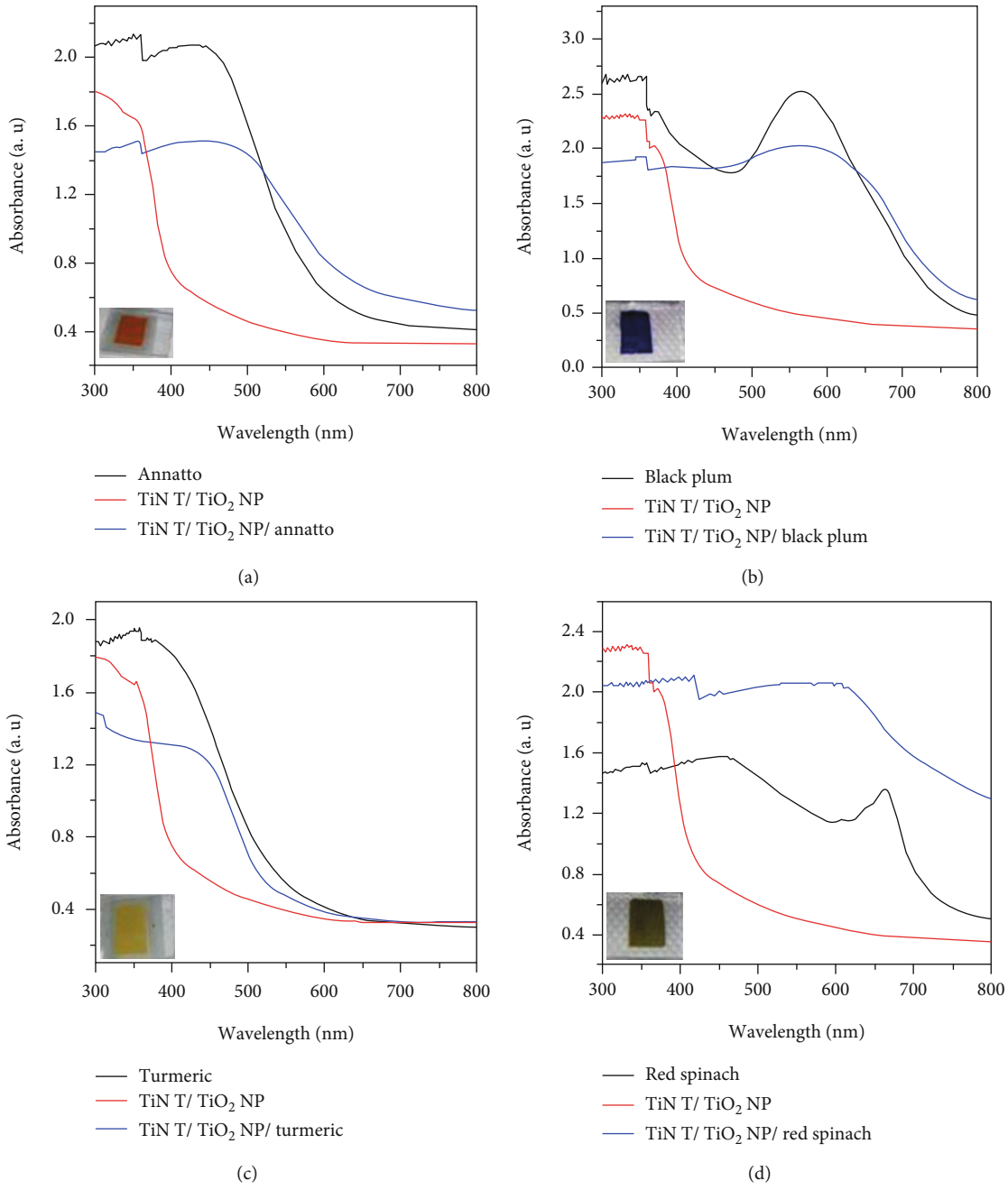

Figure 6: Continued.

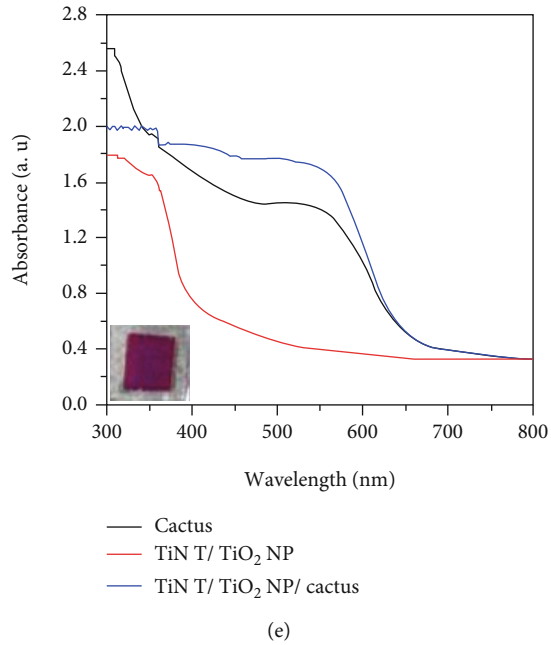

Figure 6: UV-Vis absorption spectra of dye extracts and corresponding photoanodes: (a) annatto, TiNT/TiO_2 NP, and TiNT/TiO_2 NP/annatto dye; (b) black plum, TiNT/TiO_2 NP, and TiNT/TiO_2 NP/black plum dye; (c) turmeric, TiNT/TiO_2 NP, and TiNT/TiO_2 NP/turmeric dye; (d) red spinach dye, TiNT/TiO_2 NP, and TiNT/TiO_2 NP/red spinach dye; and (e) cactus dye, TiNT/TiO_2 NP, and TiNT/TiO_2 NP/cactus dye. (Inset: photographs of corresponding dye sensitized photoanodes).

counter electrode with iodine/triiodide electrolyte between them. As soon as the electrolyte was injected, it was sealed properly to avoid any outflow of the electrolyte.

3. Result and Discussion

3.1. Characteristics of TiO_2 Nanotube-Array Electrode. Figure 2(a) shows the FESEM image of the TiO_2 NT array film after anodization of Ti foil. The nanotubes are well defined after the ultrasonic treatment of the synthesized samples. As compared with the planar film, the nanotubular assembly provides a high specific surface area for the absorption of a sufficient amount of dyes on the electrode surface followed by the crystallization obtained by the annealing of TiO_2 onto the DSSCs [29]. HRTEM images of the synthesized TiO_2NT are depicted in Figures 3(b)–3(d) and the SAED pattern in Figure 3(a). Figure 4(a) shows the FESEM image of the as formed TiO_2NT, and Figure 4(b) shows the XRD patterns of TiO_2 nanotubes annealed at 450°C. It is evidenced that TiO_2 transforms from amorphous phases to crystalline anatase phases after the annealing at 450°C.

3.2. Spectroscopic Characterization of Natural Photosensitizers

3.2.1. Annatto Dye (Bixa orellana). Annatto or *Bixa orellana* is a small tree from the family of *Bixaceae* that contains pigment bixin. From the annatto seeds, a dark-red extract is obtained, which is widely used for food colouring and flavouring. The pericarp of the seeds contains a high concentration of carotenoids and is composed of up to 80% of the carotenoid cis-bixin and the remaining 20% include trans- and cis-norbixin [30]. Cis-bixin ($C_{25}H_{30}O_4$) is insoluble in water and consists of a chain of alternating double conjugated bonds, with a carboxylic acid group at one end of the chain and a methyl ester group at the other. Norbixin ($C_{24}H_{28}O_4$) is a water soluble carotenoid with only difference is the presence of a carboxylic acid moiety in the position of the methyl ester group in bixin [30].

Figure 5(a) shows the FT-IR spectrum of annatto dye. The following assignments were made in the spectrum; at 3410 cm^{-1}, the O-H stretching vibration is observed. The C-H stretches due to methyl and methylene groups are observed at 2915 cm^{-1} and 2850 cm^{-1}, respectively. At around 1722 cm^{-1}, the carboxylic C=O group, and at 1608 cm^{-1}, the alkene C=C stretch are seen. The peaks positioned at 1438 cm^{-1} and 1378 cm^{-1} represent the C-H bending of the methyl groups, and the peak at 1287 cm^{-1} is attributed to the C-O vibrations. The peaks at 1254 cm^{-1} and 1159 cm^{-1} represent the symmetric and asymmetric vibrations of the C-O-C ester group [30, 31].

Figure 6(a) demonstrates the UV-Vis absorption spectrum of annatto dye. From the spectrum, it is observed that the annatto dye shows a wide absorption peak in the visible region (360-40 nm). With TiNT/TiO_2 NP composite, there is a widening of the peak from 360-570 nm and thereby confirms the integration of the dye into the TiNT/TiO_2 NP composite film.

3.2.2. Black Plum Fruits (Syzygium cumini). Black plum fruits (*Syzygium cumini*) are commonly found in India. The black plum fruits are deep violet or bluish in color, having various medicinal properties. The anthocyanin compounds that are present in the fruit are responsible

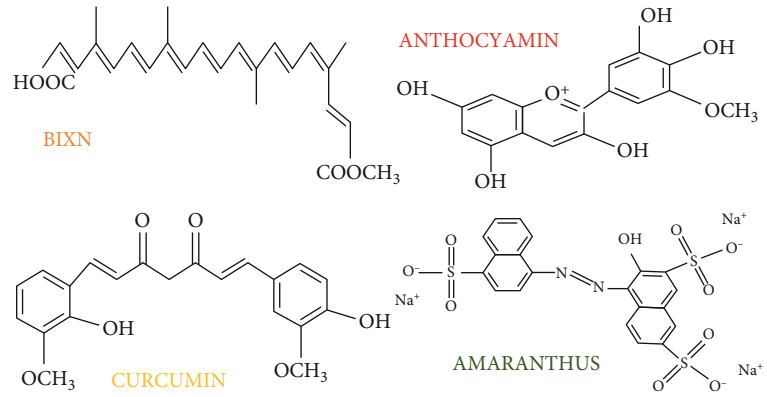

Figure 7: Chemical structures of the bixin, anthocyamin, curcumin, and amaranthus dyes.

Table 1: $J-V$ characteristic of DSSC fabricated using TiNT/TiO_2 NP photoanodes with natural dye sensitizers in comparison with the literature survey.

Natural dye	λ_{max} (nm)	V_o (V)	J_{sc} (mA/cm)^2	FF	η (%)	Ref.
Mulberry	543	0.86	0.42	0.43		[37]
Myrtus cauliflora Mart (Jaboticaba)	520	7.20	0.59	0.54	—	[38]
Red cabbage	537	0.50	0.37	0.54	0.13	[39]
Hylocereus polyrhizus (dragon fruit)	535	0.20	0.22	0.30	0.22	[40]
Bixa orellana L (annatto seeds)	474	1.1	0.57	0.59	0.37	[41]
Spinach	437	0.47	0.55	0.51	0.13	[32]
Cherries	500	0.46	0.30	38.3	0.18	[9]
Fructus lycii	447,425	0.53	0.68	46.6	0.17	[42]
Raspberries	540	0.26	0.42	64.8	1.50	[43]
Turmeric	507.2		1.857	0.503	0.473	[44]
Annatto	455	0.63	6.19	18.9	0.74	This work
Black plum	550	0.51	5.43	14.68	0.40	This work
Turmeric	425	0.62	4.59	7.99	0.22	This work
Red spinach	430 and 665	0.51	3.56	9.21	0.16	This work
Cactus	550	0.58	5.68	13.48	0.44	This work

for the violet or bluish color of the dye. The FT-IR spectroscopy studies confirmed the presence of anthocyanin pigment extracted in the black plum fruits. Figure 5(b) displays the FT-IR spectrum of the black plum fruit. The peak at 3520 cm^{-1} corresponds to the -OH stretching vibration. The peaks at 2933 cm^{-1} are assigned to the -CH stretching modes [32]. The spectral region between 1550 to 1700 cm^{-1} allows infrared absorption of C=C. Consequently, the peak at 1627 cm^{-1} corresponding to the double bond (C=C) stretching vibration could be correlated with the stretching of aromatic C=C in anthocyanin. The peaks at 1730 cm^{-1} are assigned to the C=O stretching vibration [32, 33].

Figure 6(b) explains the UV-Vis absorption spectrum of black plum dye and the dye-sensitized TiNT/TiO_2 NP photoanode. A maximum absorption is observed at 570 nm for the dye. After immersing the photoanode in the black plum dye, the photoanode films turn to blue in color (inset of Figure 6). The absorption band of the adsorbed dye was broader than the absorption band of the fresh dye solution.

3.2.3. Turmeric Dye (Curcuma longa). Turmeric rhizome root contains up to 5% essential oils and up to 3% curcumin a polyphenol. Curcumin is the active ingredient of turmeric. It exists at least in two tautomeric forms, keto and enol. The keto form is preferred in solid phase and the enol form in solution [34]. The extract of turmeric root yields a deep orange-yellow dye.

FT-IR spectrum of turmeric dye recorded in the waveband 4000-500 cm^{-1} is illustrated in Figure 5(c). The -OH stretching frequency appears at 3368 cm^{-1}. The asymmetrical C-O-C stretching frequency of aryl alkyl ethers appears at 1287 cm^{-1}. The band at 1688 cm^{-1} corresponds to the symmetrical C=O stretching of the keto group. The sharp band at 1087 cm^{-1} is assigned to the C-O-C stretch of alkyl aryl ether. The sharp band at 1039 cm^{-1} is assigned to the C-O stretch of the phenyl alkyl ether that confirms the molecular structure of curcumin extracted from turmeric [34].

Figure 6(c) reveals the UV-Vis absorption spectrum of pure curcumin and curcumin sensitized TiO_2 photoelectrode. As perceived from the curves of the absorption

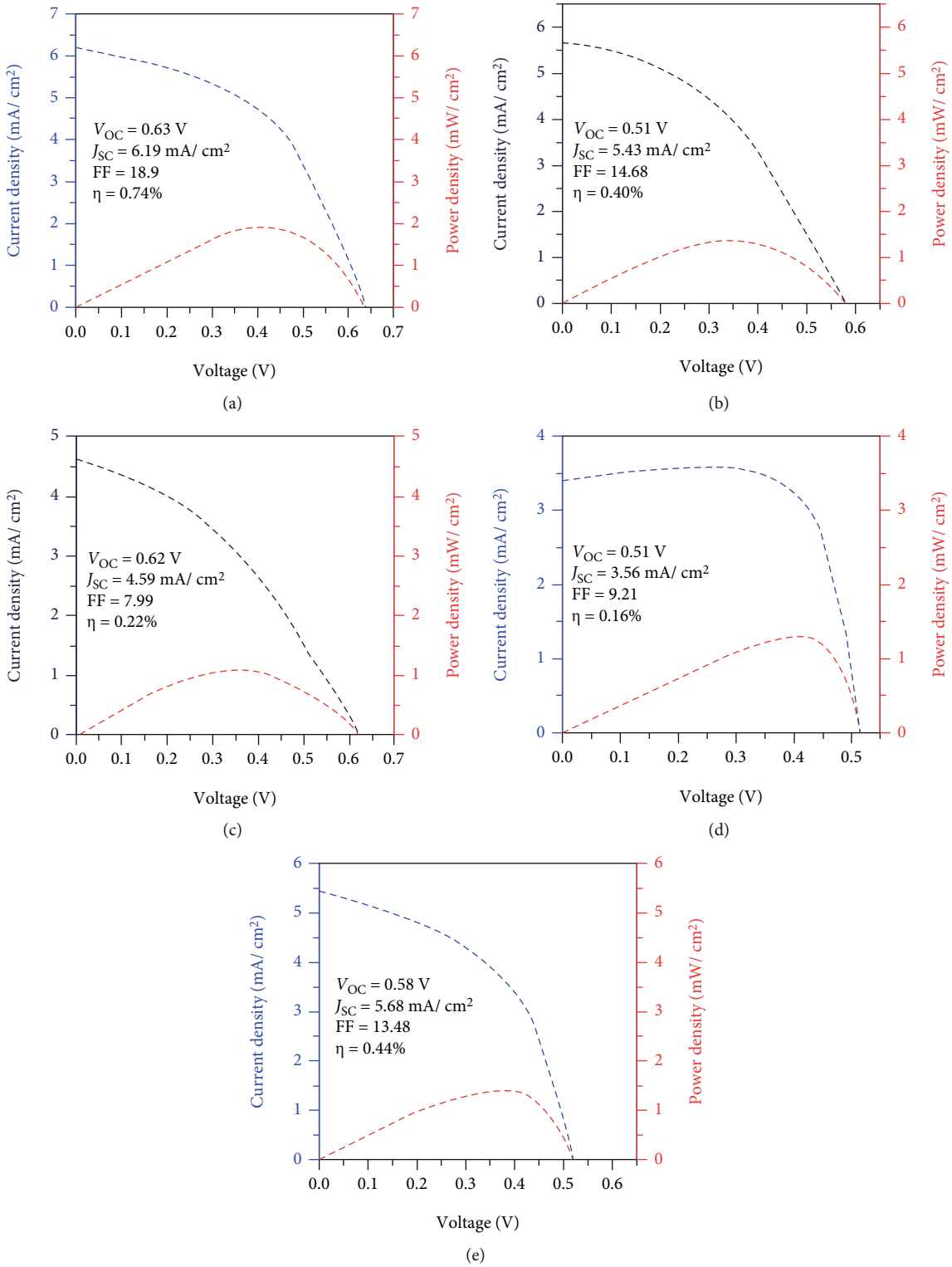

FIGURE 8: $J - V$ curves of natural DSSC: (a) annatto, (b) black plum, (c) turmeric, (d) red spinach, and (b) cactus.

spectrum, the maximum absorption peak of curcumin is at the wavelength 425 nm.

It also shows a broad peak at the wavelength range from 400 nm to 450 nm. Owing to adsorption on the TiO_2 of all pigments, the absorption band shifts to higher energy in the visible range. The broad range also indicates that the dye is stained well on the TiO_2 nanoparticles. This broadening can lead to the capacity of dye to harvest photons in a broader spectrum of solar energy, which eventually produces a higher photocurrent [34].

3.2.4. Red Spinach (Amaranthus dubius). Red spinach is a normally available vegetable in many parts of India. Its leaves are usually round thick and red in color. It also has a bright red color central stem. The leaves and stem of red spinach contain a red liquid. To extract dye from red spinach, the leaves were initially dried, crushed, and then soaked in acetone and fine green-colored dye was obtained. The red color disappeared once the leaves got dried. Figure 5(d) shows the FT-IR spectrum of red spinach dye in the spectral range within the waveband of 4000-500 cm^{-1}.

The dye extracted from red spinach exhibits the following bands corresponding to different functional groups. The peak at 3416 cm^{-1} corresponds to the -OH stretching vibration. The CH_3 and CH_2 vibrations are observed at 2930 cm^{-1} and 2817 cm^{-1}, respectively [35]. Moreover, C=O vibration at 1721 cm^{-1} and C-O vibration at 1045 cm^{-1} are also observed. The UV-Vis absorption spectrum of red spinach dye is shown in Figure 6(d). It has approximate absorption maxima at 430 and 662 nm, which were attributed to the presence of chlorophyll pigment in the extract.

3.2.5. Cactus Fruit Dye (Opunitia ficus). The fruit of the cactus, known by the name prickly pear, is in oval shape with a reddish-purple color. The reddish color is due to the presence of anthocyanin compounds. The properties of cactus fruit dye have been investigated by FT-IR and UV-Vis spectroscopic techniques.

The FT-IR spectrum of cactus dye was recorded in the spectral range of waveband 4000 cm^{-1} to 500 cm^{-1} (Figure 5(e)). From the spectrum, the broad absorption range between 3200 and 3400 cm^{-1} indicates that the chemical has an intermolecular H-bond, and the sharp peak between 1600 and 1700 cm^{-1} shows that C=O stretching vibration is conjugate. The sharp peak around 1030-1060 cm^{-1} is due to the C-O- C stretching vibration of esters acetates [35, 36].

The results prove that the due from cactus fruit contains anthocyanin which is one of the core compositions for natural dye. Chemically, cactus dye contains intermolecular H-bonds, conjugate C=O stretching, and existing ester acetates, C-O-C asymmetric stretching vibrations, all of which are caused by the anthocyanin component [36]. The carbonyl and hydroxyl groups in cactus fruit dye can be bound with the surface of TiO_2 and thus result in photoelectric effects.

The absorption spectrum of cactus fruit was obtained in the wavelength range between 300 nm and 800 nm using UV-Vis spectroscopy. In Figure 6(e), the cactus dye is found to have an absorption peak at 535 nm and show a good absorption level between 450 and 600 nm. The structures of the dye based on the natural sources are depicted in Figure 7.

3.3. Photoelectrochemical Performance of DSSCs Sensitized with Natural Dyes. In the presence of white light emitted(100 mW cm^{-2}) from the solar simulator, the DSSC with the natural dyes was studied. The performance of DSSC using natural dye sensitizers was evaluated by short circuit current density (J_{sc}), open-circuit voltage (V_{oc}), fill factor (FF), and energy conversion efficiency (η). The $J - V$ characteristics of the DSSC sensitized with natural dyes are listed in Table 1. Figures 8(a)–8(f) show the photocurrent photovoltage ($J - V$) characteristics of the DSSCs, and the fill factors of these DSSC are found to be very low. The V_{oc} varies from 0.51 to 0.63 V, and the J_{sc} changes from 3.56 to 6.19 mA cm^{-2}. Specifically, a high V_{oc} (0.63 V) and J_{sc} (6.19 mA cm^{-2}) were obtained from the DSSC sensitized by the annatto dye, where the efficiency of the DSSC reached up to 0.7%.

4. Conclusion

An investigation on the use of natural dyes as photosensitizers for DSSC fabrication was taken up in this study. Natural dye-based solar cells appear to be limited by low V_{oc} and J_{sc}. Though the studies cornered with the natural dyes are still below the necessary requirements, the obtained results are highly encouraging and could also pave way for new natural dyes or modification to the present ones. The environmental friendliness and low-cost production make it a promising candidate for natural dyes as sensitizers.

Data Availability

The data supporting this work is available from the corresponding author upon request.

Conflicts of Interest

The authors declare that they have no conflicts of interest.

References

[1] B. O'Regan and M. Grätzel, "A low-cost, high-efficiency solar cell based on dye-sensitized colloidal TiO_2 films," *Nature*, vol. 353, no. 6346, pp. 737–740, 1991.

[2] M. Grätzel, "Solar energy conversion by dye-sensitized photovoltaic cells," *Inorganic Chemistry*, vol. 44, no. 20, pp. 6841–6851, 2005.

[3] G. George, R. S. Yendaluru, and A. Mary Ealias, "Fabrication of dye-sensitized solar cells using natural flower dye extracts: a study on performance analysis and solar dye degradation," *Energy Sources, Part A: Recovery, Utilization, and Environmental Effects*, vol. 42, pp. 1–15, 2020.

[4] D. Pan, J. Jiao, Z. Li et al., "Efficient separation of electron–hole pairs in graphene quantum dots by TiO2Heterojunctions for dye degradation," *ACS Sustainable Chemistry & Engineering*, vol. 3, no. 10, pp. 2405–2413, 2015.

[5] D. Sampaio, R. S. Babu, H. R. M. Costa, and A. L. F. de Barros, "Investigation of nanostructured TiO2 thin film coatings for DSSCs application using natural dye extracted from jabuticaba fruit as photosensitizers," *Ionics (Kiel)*, vol. 25, no. 6, pp. 2893–2902, 2018.

[6] A. Kay and M. Graetzel, "Artificial photosynthesis. 1. Photosensitization of titania solar cells with chlorophyll derivatives and related natural porphyrins," *The Journal of Physical Chemistry*, vol. 97, no. 23, pp. 6272–6277, 1993.

[7] G. P. Smestad and M. Gratzel, "Demonstrating electron transfer and nanotechnology: a natural dye-sensitized nanocrystalline energy converter," *Journal of Chemical Education*, vol. 75, no. 6, pp. 752–756, 1998.

[8] S. Hao, J. Wu, Y. Huang, and J. Lin, "Natural dyes as photosensitizers for dye-sensitized solar cell," *Solar Energy*, vol. 80, no. 2, pp. 209–214, 2006.

[9] A. Polo and N. Murakamiiha, "Blue sensitizers for solar cells: natural dyes from Calafate and Jaboticaba," *Solar Energy Materials & Solar Cells*, vol. 90, no. 13, pp. 1936–1944, 2006.

[10] E. Yamazaki, M. Murayama, N. Nishikawa, N. Hashimoto, M. Shoyama, and O. Kurita, "Utilization of natural carotenoids as photosensitizers for dye-sensitized solar cells," *Solar Energy*, vol. 81, no. 4, pp. 512–516, 2007.

[11] M. S. Roy, P. Balraju, M. Kumar, and G. D. Sharma, "Dye-sensitized solar cell based on Rose Bengal dye and nanocrystalline TiO_2," *Solar Energy Materials & Solar Cells*, vol. 92, no. 8, pp. 909–913, 2008.

[12] K. Wongcharee, V. Meeyoo, and S. Chavadej, "Dye-sensitized solar cell using natural dyes extracted from rosella and blue pea flowers," *Solar Energy Materials & Solar Cells*, vol. 91, no. 7, pp. 566–571, 2007.

[13] G. Calogero and G. D. Marco, "Red Sicilian orange and purple eggplant fruits as natural sensitizers for dye- sensitized solar cells," *Solar Energy Materials & Solar Cells*, vol. 92, no. 11, pp. 1341–1346, 2008.

[14] D. Zhang, S. M. Lanier, J. A. Downing, J. L. Avent, J. Lum, and J. L. McHale, "Betalain pigments for dye-sensitized solar cells," *Journal of Photochemistry and Photobiology A: Chemistry*, vol. 195, no. 1, pp. 72–80, 2008.

[15] M. A. M. al-Alwani, N. A. Ludin, A. B. Mohamad, A. A. H. Kadhum, and A. Mukhlus, "Application of dyes extracted from *Alternanthera dentata* leaves and *Musa acuminata* bracts as natural sensitizers for dye-sensitized solar cells," *Spectrochimica Acta Part A: Molecular and Biomolecular Spectroscopy*, vol. 192, pp. 487–498, 2018.

[16] G. R. A. Kumara, S. Kaneko, M. Okuya, B. Onwona-Agyeman, A. Konno, and K. Tennakone, "Shiso leaf pigments for dye-sensitized solid-state solar cell," *Solar Energy Materials & Solar Cells*, vol. 90, no. 9, pp. 1220–1226, 2006.

[17] Y. S. Yen, Y. C. Chen, H. H. Chou, S. T. Huang, and J. T. Lin, "Novel organic sensitizers containing 2, 6-difunctionalized anthracene unit for dye sensitized solar cells," *Polymers (Basel)*, vol. 4, no. 3, pp. 1443–1461, 2012.

[18] D. Joly, L. Pellejà, S. Narbey et al., "A robust organic dye for dye sensitized solar cells based on iodine/iodide electrolytes combining high efficiency and outstanding stability," *Scientific Reports*, vol. 4, no. 1, p. 4033, 2014.

[19] A. Dessì, M. Calamante, A. Mordini et al., "Organic dyes with intense light absorption especially suitable for application in thin-layer dye-sensitized solar cells," *Chemical Communications*, vol. 50, no. 90, pp. 13952–13955, 2014.

[20] J. V. Vaghasiya, K. K. Sonigara, J. Prasad, M. Qureshi, S. C. Tan, and S. S. Soni, "Contribution in light harvesting by solid ionic conductors for efficient photoelectrochemical cells: an effect of an identical donor molecule in sensitizers and electrolytes," *ACS Applied Energy Materials*, vol. 3, no. 7, pp. 7073–7082, 2020.

[21] A. M. Ammar, H. S. H. Mohamed, M. M. K. Yousef, G. M. Abdel-Hafez, A. S. Hassanien, and A. S. G. Khalil, "Dye-sensitized solar cells (DSSCs) based on extracted natural dyes," *Journal of Nanomaterials*, vol. 2019, Article ID 1867271, 10 pages, 2019.

[22] H. Hug, M. Bader, P. Mair, and T. Glatzel, "Biophotovoltaics: natural pigments in dye-sensitized solar cells," *Applied Energy*, vol. 115, pp. 216–225, 2014.

[23] R. Kushwaha, P. Srivastava, and L. Bahadur, "Natural pigments from plants used as sensitizers for TiO_2 based dye-sensitized solar cells," *Journal of Energy*, vol. 2013, Article ID 654953, 8 pages, 2013.

[24] G. Calogero, J.-H. Yum, A. Sinopoli, G. Di Marco, M. Grätzel, and M. K. Nazeeruddin, "Anthocyanins and betalains as light-harvesting pigments for dye-sensitized solar cells," *Solar Energy*, vol. 86, no. 5, pp. 1563–1575, 2012.

[25] W. A. Ayalew and D. W. Ayele, "Dye-sensitized solar cells using natural dye as light-harvesting materials extracted from *Acanthus sennii chiovenda* flower and *Euphorbia cotinifolia* leaf," *Journal of Science: Advanced Materials and Devices*, vol. 1, no. 4, pp. 488–494, 2016.

[26] K. K. Sonigara, J. V. Vaghasiya, J. Prasad et al., "Augmentation in photocurrent through organic ionic plastic crystals as an efficient redox mediator for solid-state mesoscopic photovoltaic devices," *Sustainable Energy Fuels*, vol. 5, no. 5, pp. 1466–1476, 2021.

[27] R. Beranek, H. Hildebrand, and P. Schmuki, "Self-organized porous titanium oxide prepared in H_2 SO_4/HF electrolytes," *Electrochemical and Solid-State Letters*, vol. 6, no. 3, p. B12, 2003.

[28] T. Berger, T. Lana-Villarreal, D. Monllor-Satoca, and R. Gómez, "An electrochemical study on the nature of trap states in nanocrystalline rutile thin films," *Journal of Physical Chemistry C*, vol. 111, no. 27, pp. 9936–9942, 2007.

[29] K. Bhattacharyya, A. Danon, B. K. Vijayan, K. A. Gray, P. C. Stair, and E. Weitz, "Role of the surface Lewis acid and base sites in the adsorption of CO2on titania nanotubes and platinized titania nanotubes: an in situ FT-IR study," *Journal of Physical Chemistry C*, vol. 117, no. 24, pp. 12661–12678, 2013.

[30] S. Joseph, S. J. Melvin Boby, D. M. G. Theresa Nathan, and P. Sagayaraj, "Investigation on the role of cost effective cathode materials for fabrication of efficient DSSCs with TiNT/TiO_2 nanocomposite photoanodes," *Solar Energy Materials & Solar Cells*, vol. 165, pp. 72–81, 2017.

[31] Q. Chen and D. Xu, "Large-scale, noncurling, and free-standing crystallized TiO2 nanotube arrays for dye-sensitized solar cells," *Journal of Physical Chemistry C*, vol. 113, no. 15, pp. 6310–6314, 2009.

[32] N. M. Gómez-Ortíz, I. A. Vázquez-Maldonado, A. R. Pérez-Espadas, G. J. Mena-Rejón, J. A. Azamar-Barrios, and G. Oskam, "Dye-sensitized solar cells with natural dyes extracted from achiote seeds," *Solar Energy Materials & Solar Cells*, vol. 94, no. 1, pp. 40–44, 2010.

[33] T. Lóránd, P. Molnár, J. Deli, and G. Tóth, "FT-IR study of some seco- and apocarotenoids," *Journal of Biochemical and Biophysical Methods*, vol. 53, no. 1-3, pp. 251–258, 2002.

[34] C. S. Pappas, C. Takidelli, E. Tsantili, P. A. Tarantilis, and M. G. Polissiou, "Quantitative determination of anthocyanins in three sweet cherry varieties using diffuse reflectance infrared Fourier transform spectroscopy," *Journal of Food Composition and Analysis*, vol. 24, no. 1, pp. 17–21, 2011.

[35] J. Srivastava and P. S. Vankar, "*Canna indica* flower: new source of anthocyanins," *Plant Physiology and Biochemistry*, vol. 48, no. 12, pp. 1015–1019, 2010.

[36] H. J. Kim, D. J. Kim, S. N. Karthick et al., "Curcumin dye extracted from curcuma longa L. used as sensitizers for efficient dyesensitized solar cells," *International Journal of Electrochemical Science*, vol. 8, 2013.

[37] M. Alhamed, A. S. Issa, and A. W. Doubal, "Studying of natural dyes properties as photo-sensitizer for dye sensitized solar cells (DSSC)," *Journal of the Electron Devices*, vol. 16, pp. 1370–1383, 2012.

[38] H. Zhou, L. Wu, Y. Gao, and T. Ma, "Dye-sensitized solar cells using 20 natural dyes as sensitizers," *Journal of Photochemistry and Photobiology A: Chemistry*, vol. 219, no. 2-3, pp. 188–194, 2011.

[39] K. E. Jasim, S. A. Dallal, and A. M. Hassan, "Natural dye-sensitised photovoltaic cell based on nanoporous TiO_2," *International Journal of Nanoparticles*, vol. 4, no. 4, pp. 359–368, 2011.

[40] H. Chang, H. M. Wu, T. L. Chen, K. D. Huang, C. S. Jwo, and Y. J. Lo, "Dye-sensitized solar cell using natural dyes extracted from spinach and ipomoea," *Journal of Alloys and Compounds*, vol. 495, no. 2, pp. 606–610, 2010.

[41] A. Dumbrava, A. Georgescu, G. Badea, I. Enache, C. Orrea, and M. A. Girtu, "Dyesensitized solar cells based on nanocrystalline TiO2 and natural pigments," *Journal of Optoelectronics and Advanced Materials*, vol. 10, pp. 2996–3002, 2008.

[42] R. A. M. Ali and N. Nayan, "Fabrication and analysis of dye-sensitized solar cell using natural dye extracted from dragon fruit," *The International Journal of Integrated Engineering*, vol. 2, pp. 55–62, 2010.

[43] C. G. Garcia, A. S. Polo, and N. Y. Murakami Iha, "Fruit extracts and ruthenium polypyridinic dyes for sensitization of TiO_2 in photoelectrochemical solar cells," *Journal of Photochemistry and Photobiology A: Chemistry*, vol. 160, no. 1-2, pp. 87–91, 2003.

[44] F. Kabir, S. Nazmus Sakib, S. Shehab Uddin, E. Tawsif Efaz, and M. T. Farhan Himel, "Enhance cell performance of DSSC by dye mixture, carbon nanotube and post $TiCl_4$ treatment along with degradation study," *Sustainable Energy Technologies and Assessments*, vol. 35, pp. 298–307, 2019.

Hindawi
Journal of Nanomaterials
Volume 2021, Article ID 5551148, 11 pages
https://doi.org/10.1155/2021/5551148

Research Article

Enhanced Photocatalytic Degradation of Phenol Using Urchin-Like ZnO Microrod-Reduced Graphene Oxide Composite under Visible-Light Irradiation

S. Mary Margaret, Albin John P. Paul Winston, S. Muthupandi, P. Shobha, and P. Sagayaraj

Loyola College (Autonomous), Nungambakkam, Chennai, Tamil Nadu, India

Correspondence should be addressed to P. Sagayaraj; sagayaraj1962@gmail.com

Received 2 February 2021; Revised 8 June 2021; Accepted 26 June 2021; Published 26 July 2021

Academic Editor: Baskaran Rangasamy

In this study, visible-light-driven ZnO microrod-rGO heterojunction composites were successfully synthesized via a facile and scalable hydrothermal process. The prepared photocatalyst heterojunction was examined using different techniques including XRD, SEM, FTIR, UV-Vis spectroscopy, and TGA to reveal their crystal phase, morphology, and other optical properties. The photocatalytic performance of the obtained ZnO-rGO composites was measured by the photodegradation of phenol under visible light illumination. The addition of graphene over the catalyst exhibited an enhanced photocatalytic activity for phenol degradation due to its high surface area and decreasing rate of electron-hole separation. Kinetic studies proved that the degradation of phenol process happened by following the pseudo-first-order kinetic model. The effective conditions for degradation of phenol using ZnO-rGO composite were 0.2 g L^{-1}catalyst dose, pH -4, and initial concentration 20 ppm of phenol solution. Comparing with ZnO microrods, the heterojunction composite degraded the organic pollutants of phenol solution up to 84.2% of efficiency displaying the highest photocatalytic activity, whereas urchin-like ZnO catalyst exhibited much less photocatalytic activity for phenol degradation under visible light irradiation. This result envisages immense properties, showing a great potential industrial application for the removal of phenolic wastewater.

1. Introduction

In today's industrialization, environmental pollution has been booming day by day. Industries that use plenty of water include textile companies, refining petroleum, automotive manufacturing, and primary metals [1]. The discharge from these industries produces plenty of organic contamination which makes severe damages to the ecosystem especially to the aqueous system by decreasing the concentration of oxygen dissolved in the environment. Among the biorecalcitrant toxic compounds, phenol is the most harmful organic compound which is a ubiquitous water pollutant that plays a vital role in industries such as pharmaceuticals, coal conversion, paint, cresols, dyeing, and pulpmill [2]. The European Union regulation has declared the maximum permitted amount of phenolic compounds in freshwater as 0.5 mg L^{-1} [3].

Therefore, there has been a growing interest to eliminate these contaminations from the industrial water and make it usable for the ecological systems like plant, animal, and human beings. Thus, researchers have done a lot of work to develop fascinating methods for the removal of water pollutants in this area including the approaches like ion floatation, sonocatalytic degradation, photocatalytic degradation, swirling jet-induced method, hydrodynamic cavitation, electrochemical oxidation, and advanced oxidation processes [4–11]. Among these, heterogeneous photodegradation is the most remarkable and effective method for converting toxic organic pollutants into carbonaceous products [12].

Nowadays, many researchers prefer heterogeneous photodegradation process owing to its good electron conductivity, huge specific surface area, material consumption, high stability, high absorption, conduction empty band (CB), and

electronic structure packed valance band (VB) [13–16]. The method of phenol degradation through semiconducting metal oxide has been under usage as photocatalyst materials involving TiO_2 [17], ZnO [18], V_2O_5 [19], Fe_3O_4 [20], and MgO [21] and is well known and ascribed to the arrangement of electron-hole pair at the valance and conduction band after absorption of less amount of energy from UV or visible light.

Among semiconducting nano/microstructure, ZnO is a promising candidate with suitable bandgap energy of ~3.4 eV and versatile material for photodegradation under the removal of various types of organic dyes in an aqueous or gaseous medium [22]. It has been confirmed that ZnO can exhibit high photocatalytic degradation than TiO_2 for some dyes owing to its economic viability and ecofriendly nature [23]. These are diverse experimental methods for the synthesis of ZnO-rGO heterojunction materials [24], including solvothermal, hydrothermal, microwave synthesis, electrochemical deposition, precipitation method, and solution combustion synthesis. In this paper, a hydrothermal approach was used for synthesizing urchin-like ZnO with the addition of graphene material with the idea to enhance the photocatalytic performance. Furthermore, the morphology plays a significant role for the better performance of photocatalytic activity. In the recent studies, hierarchically ordered ZnO microstructures are found to exhibit high photocatalytic performance due to their high stability against aggregation and large specific surface area [25, 26]. Literature reviews suggest that graphene sheet enhances various properties such as large values of Young modulus, extremely high surface area, high visible light optical transparency, superior mobility of charge carriers (200,000 $cm^2 V^{-1} s^{-1}$), and thermal conductivity [27, 28]. Thus, reduced graphene oxide-(rGO-) based metal oxide photocatalytic materials have recently gained a lot of attention among the scientists to improve the charge transfer at the interface; it reduces the recombination of charge carriers on the surface of catalysts and offers high performance to absorb pollutants. These multifunctional heterojunctions have been demonstrated to be outstanding candidate fruits in fields like photocatalytic degradation of organic pollutants over visible light irradiation. Research has been conducted for several decades on ZnO-based nanocomposite due to its better photocatalytic performance and high surface area, but the complexity to recover from the reaction system and agglomeration are two major problems that restrict its practical application [29, 30]. Thus, microsized ZnO with a high surface area is an alternative pathway to overcome these problems.

For instance, Qin et al. reported ZnO microsphere-rGO nanocomposites for photodegradation of methylene blue pigment under UV irradiation [31]. Pant et al. synthesized ZnO microflowers arranged on reduced graphene oxide of MB dye over UV irradiation [32]. To the best of our knowledge, there are limited works which used urchin-like ZnO microrod-rGO composites as a heterojunction for degradation of phenol in visible light irradiation. Herein, we report the synthesis of urchin-like ZnO microrod-rGO composites by a facile and environmentally friendly hydrothermal method. The synthesized composite was examined and characterized for photocatalytic degradation of phenol under visible light illumination. Moreover, the effect of special parameters including optical, magnetic, photoconductivity, phenol concentration, catalyst dosage, and photocatalytic properties of urchin-like ZnO microrod-rGO composite was also investigated.

2. Materials and Methods

2.1. Materials. Graphite, zinc nitrate hexahydrate ($Zn(NO_3)_2{\cdot}6H_2O$), polyethylene glycol (PEG 4000), ammonium hydroxide ($NH_3{\cdot}H_2O$), potassium persulfate ($K_2S_2O_8$), sulfuric acid (H_2SO_4), phosphorus pentoxide (P_2O_5), hydrochloric acid (HCl), potassium permanganate ($KMnO_4$), ethylene glycol ($C_2H_6O_2$), hydrogen peroxide (H_2O_2), and ascorbic acid ($C_6H_8O_6$) were purchased from Aldrich and used as received.

2.2. Preparation of Graphene Oxide (GO). Graphene oxide was synthesized from graphite powder by using the modified Hummers method [33]. Typically, 3 g of graphite, 2 g of P_2O_5, and 2 g of $K_2S_2O_8$ were added into 24 mL of concentrated H_2SO_4 under stirring at 95°C for 6 h. The mixture was cooled down to normal room temperature and 1 L of deionized (DI) water was added into the mixture and kept under ageing for 48 h. The mixture was then washed, filtered, and dried out to obtain the black powder. Subsequently, 15 g of $KMnO_4$ and 125 mL of concentrated H_2SO_4 were added into the mixture and kept in an ice bath below 10°C and magnetically stirred at 40°C for 3 h. The obtained grey sample was diluted with the dropwise addition of 10 mL of H_2O_2 followed by the slow addition of 0.5 L of DI water to quench the solution, and the colour of the solution became yellowish. The obtained product was centrifuged, cleaned with HCl to remove impurities, and washed with DI water. The final product was dried at 40°C in a vacuum oven to attain the GO sample.

2.3. Preparation of Reduced Graphene Oxide (rGO). Reduced graphene oxide (rGO) was synthesized from graphite oxide (GO) by using ascorbic acid as a reductant [34]. 0.1 mg/mL of GO solution and 0.1 M ascorbic acid were mixed and kept at 70°C on a heating shield and stirred for 35 min; the colour of the solution turned from yellow to black. The product was centrifuged and dried at 120°C in a vacuum.

2.4. Preparation of the Urchin-Like ZnO Microrod-rGO Composite Materials. In a typical experiment, 10.8 g $Zn(NO_3)_2{\cdot}6H_2O$, 2.5 wt. % of rGO, 30 mL of $C_2H_6O_2$, and 0.6 g PEG 4000 were dissolved in distilled water (120 mL). Then, $NH_3{\cdot}H_2O$ was added dropwise until the pH adjusted to 8. After being magnetically stirred for 35 min, the solution was transferred into a 250 mL Teflon-lined stainless steel autoclave. The autoclave was kept at 120°C for 24 h in an oven and then cooled down to the room temperature naturally. The product was washed with distilled water and absolute ethanol several times and dried at 60°C for 24 h.

Finally, the product of urchin-like ZnO microrod-rGO was obtained.

2.5. Evaluation of Photocatalytic Activity. The degradation reaction of urchin-like ZnO microrod-rGO of the prepared catalysts was conducted by measuring the photodegradation of the phenol in aqueous solution (10 mg/L) under visible light illumination at ambient temperature. The adsorption process was kept under a dark region as a batch process. Typically, 30 mg of photocatalyst was added to 50 mL of the aqueous solution and stirred for some time to evade residue of the catalyst. Prior to irradiation, the experimental set-up was placed in a complete dark portion and magnetically stirred for 60 min in the dark to achieve adsorption-desorption equilibrium. Subsequently, the photocatalytic reaction was in progress by the exposure of a 50 W tungsten lamp as a visible light source. The distance between source and photoreaction sample was 20 cm, and 5 mL of sample was taken out with the help of a syringe (~5 mL) at time interval of each 15 min. The mixture solutions were then centrifuged, and the supernatant of the dye was analysed by using a UV-Vis spectrophotometer (Shimadzu 2450 series, Japan). The degradation efficiency of the phenol can be defined as follows:

$$D(\%) = \left(\frac{1 - C_t}{C_0}\right) \times 100\%, \quad (1)$$

where C_0 is the initial dye concentration (mg/L) at time $t = 0$ and C_t is the residual concentration of phenol (mg/L) at different irradiation intervals t, respectively. The photodegradation follows pseudo-first-order kinetics, which can be expressed as follows:

$$-\ln\left(\frac{C_t}{C_0}\right) = k_{\text{app}} t, \quad (2)$$

where k (min^{-1}) is the rate constant of photodegradation [35].

2.6. Characterization. The X-ray diffractogram patterns of the prepared samples were recorded using an X-ray diffraction system (XRD 3003 TT) from 10 to 70° with Cu Kα (1.5406 Å) radiation. High-resolution scanning electron microscopy (HRSEM) was employed for morphological study by using GMS 5900, JEOL, Japan. Fourier transform infrared (FT-IR) spectrum studies were recorded using a PerkinElmer Spectrum 2 spectrometer in the wavenumber ranging from 4000 to 400 cm^{-1}. Thermogravimetric (TGA) analysis was carried with the instrument (NETZSCH STA 449F3, Germany), to investigate the stability of samples at higher temperatures. A UV-Vis spectrometer (PerkinElmer Lambda 25) was used to collect the UV-visible absorption spectra of the dye samples.

3. Results and Discussion

3.1. X-Ray Diffraction Analysis. The recorded powder XRD patterns of the as-prepared rGO, ZnO, and the ZnO-rGO composite is shown in Figure 1. The diffraction pattern of rGO shows a broad peak at 2θ value 25.6° corresponding to the (002) planes of interlayer distance of 3.47 Å [36]. The XRD peak of ZnO shows sharp and intense diffraction peaks at 2θ of 31.5°, 34.1°, 36°, 47.2°, 56.3°, 62.6°, 66.1°, 67°, and 68.8°

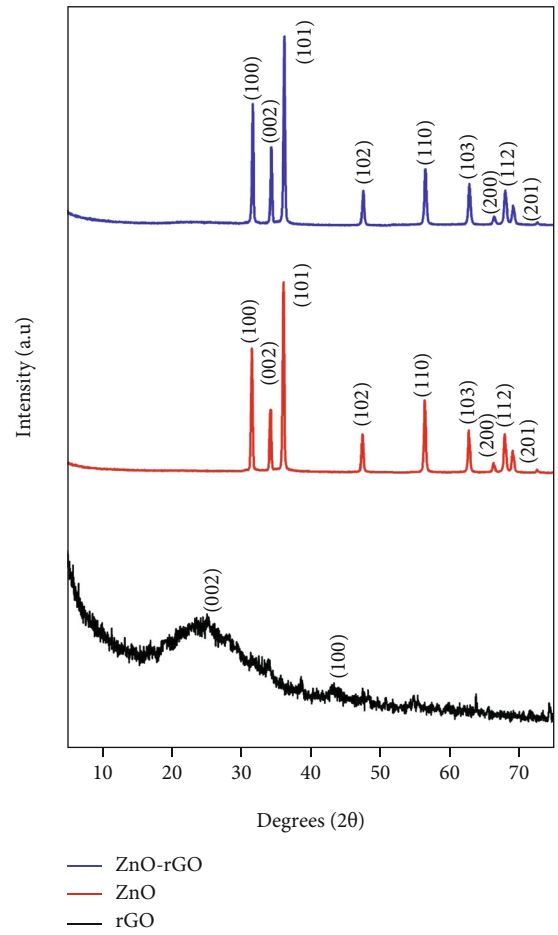

Figure 1: X-ray patterns of the rGO, ZnO, and ZnO-rGO composites.

and its corresponding lattice planes (100), (002), (101), (102), (110), (103), (002), (112), and (201), respectively. The as-prepared urchin-like ZnO microstructure exhibited good crystalline nature with hexagonal wurtzite structure and is in agreement with the standard JCPDS card No: 36-1451 [37]. In addition, the ZnO-rGO composite reveals a similar XRD pattern of ZnO-related diffraction peaks with the rGO-related wide peak that confirms the heterojunction structure. However, the rGO peak is not seen in the ZnO-rGO composite due to the relatively less intensity [38]. No proof of any other impurities is detected conforming that the ZnO-rGO composite is successfully prepared.

3.2. Morphological Analysis. The morphologies and microstructures of rGO, urchin-like ZnO, and ZnO microrod-rGO composites were investigated via HR-SEM and shown in Figures 2(a)–2(d), respectively. The compact wrinkled-like rGO sheet confirms the formation of the 2D structure which clearly indicates that the graphene oxide has been well reduced during the hydrothermal process (Figure 2(a)) [35]. The pure urchin-like ZnO (Figures 2(b) and 2(c)) with a diameter of about 10 μm is self-assembled by micro/nanorods. It has a length of approximately 3-5 μm and a diameter of 600-800 nm as shown in Figure 2(c). The network of

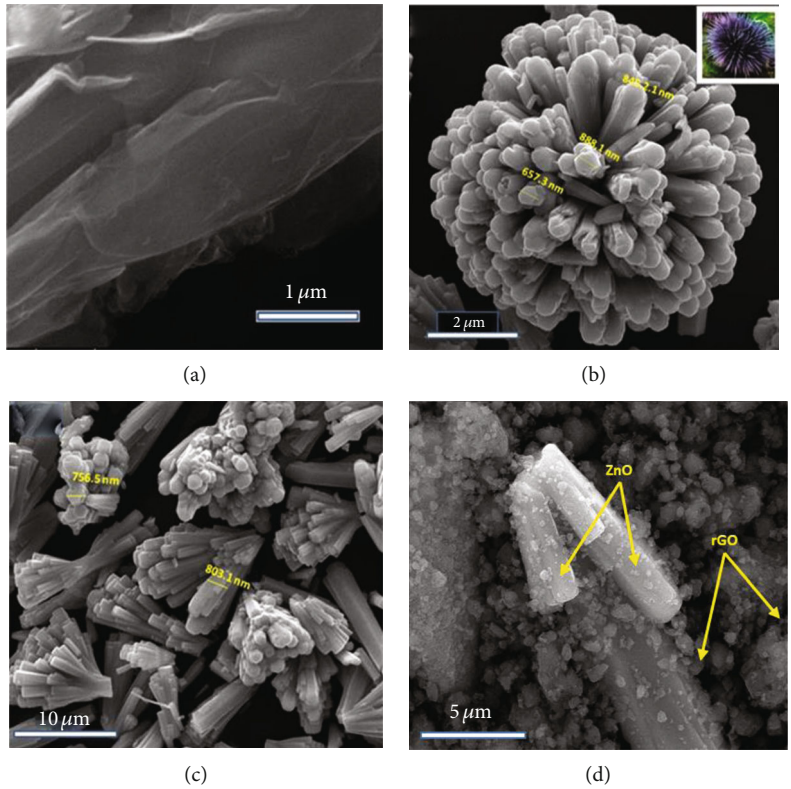

Figure 2: SEM images of (a) rGO, (b, c) urchin-like ZnO microrods, and (d) ZnO microrod-rGO composite.

urchin-like ZnO also shows a compact distribution of nanorods, and hence, it caused the well-ordered shape of nanorods. In the SEM image of ZnO-rGO (Figure 2(d)), it can be identified that urchin-like ZnO micro/nanorods are anchored and well dispersed on the rGO sheet. After the growth of ZnO micro/nanostructures on the rGO, the graphene has changed its morphology due to larger size of ZnO particles. Hence, the larger size of composites will enhance a conductive to recycling and the more channels in the nanorods will provide better transportation of electrons during the process of photodegradation [39].

3.3. Fourier Transform Infrared (FT-IR) Analysis. Figure 3 shows the FT-IR spectra of rGO, urchin-like ZnO, and ZnO-rGO composite. All samples exhibit a strong and wide absorption peak around 3200-3500 cm^{-1} which is attributed to the stretching of O-H vibration of the amide group [40]. In the case of rGO, we observed that the absorption bands decreased distinctly to less intensity and oxygen functionalities disappeared, which conforms the surface of GO has been reduced to rGO [41]. Besides, the strong peaks at 459 cm^{-1} are assigned to the stretching vibration of the Zn-O hexagonal phase [42]. The absorption peaks at 1627 cm^{-1}, 1385 cm^{-1}, and 893 cm^{-1} correspond to the aromatic C=C bond and skeletal ring vibrations from the graphitic domain, C-OH stretching vibrations, and bending vibration of C–OH, respectively [40, 43]. But after hydrothermal reaction, the intensity of the peak significantly decreased. However, this peak was red shifted to 534 cm^{-1} in the ZnO-rGO composite due to interactions between the urchin-like ZnO microstructure and residual epoxy and hydroxyl functional groups of the rGO [40, 44, 45].

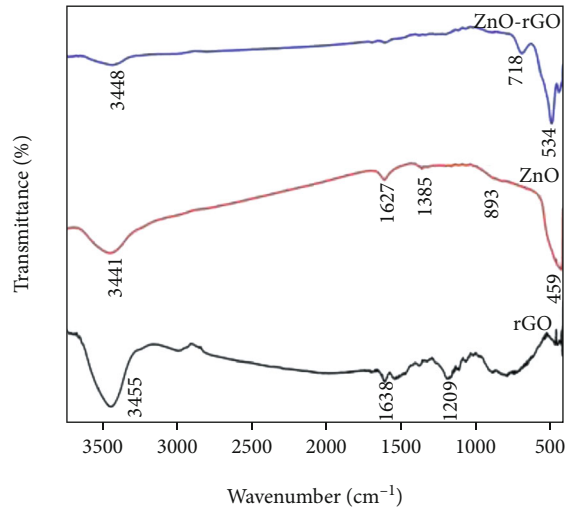

Figure 3: FT-IR spectra of the rGO, ZnO, and ZnO-rGO composites.

3.4. UV-Visible Absorbance Analysis. To examine the optical properties of the as-synthesized materials, UV-Vis optical absorption spectra were recorded (Figure 4(a)). It is an effective way to study about surface defects and is strongly associated with the photocatalytic activity of ZnO-rGO composites [46]. The strong characteristic absorbance peak at about 377 nm indicated highly crystalline and inherent bandgap

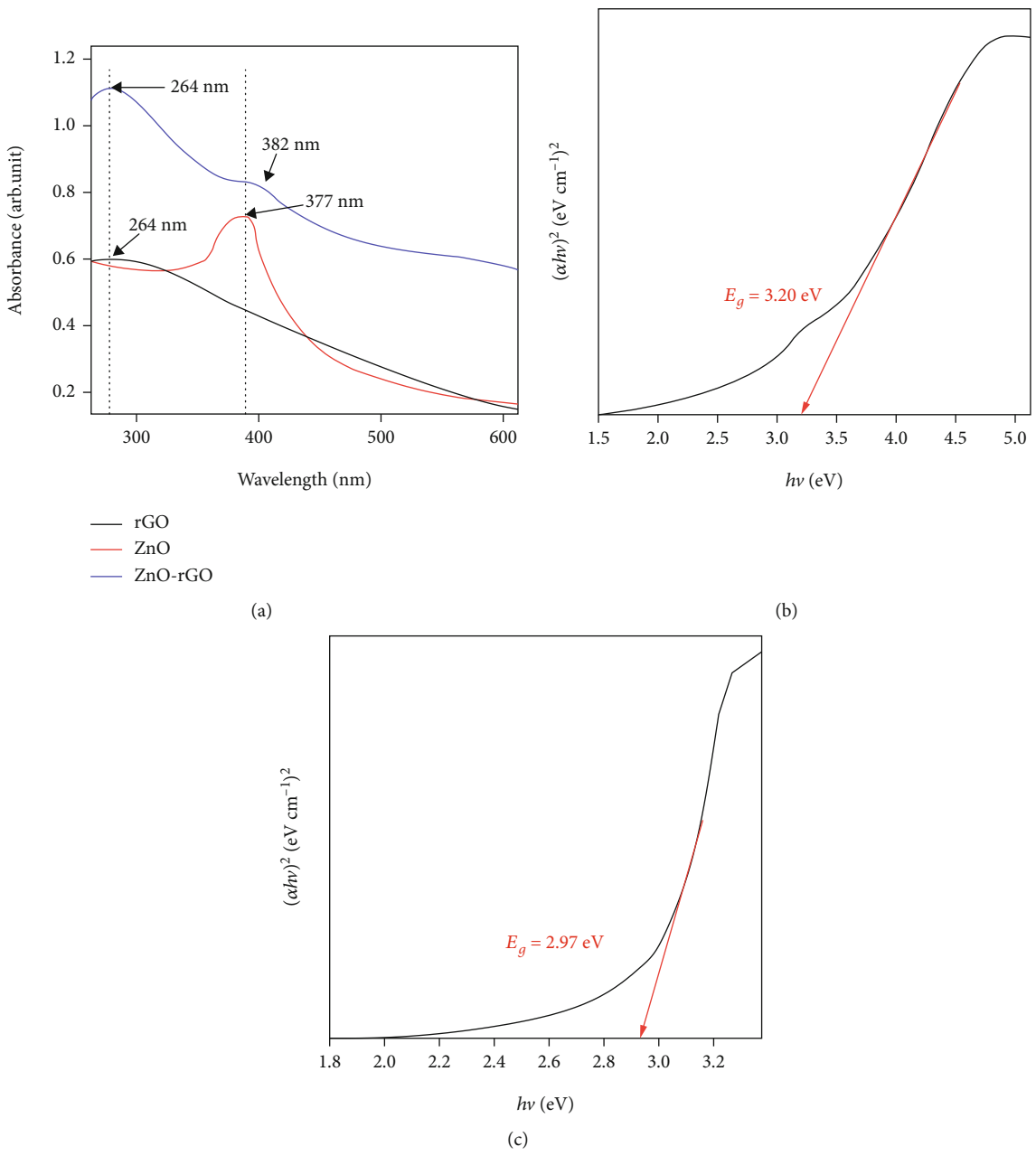

FIGURE 4: (a) UV-visible absorbance spectra for the as-synthesized rGO, ZnO, and ZnO-rGO; (b, c) Tauc plot to examine the bandgap of ZnO and ZnO-rGO.

absorption of ZnO particles [28]. rGO shows the absorption peak seen at 264 nm and is attributed to $\pi - \pi *$ orbital transition [47], while the characteristic spectra of ZnO-rGO composites show a peak at 264 nm which belongs to the rGO, and another absorption peak at 382 nm is attributed to ZnO microstructure. Therefore, the ZnO in the composite material got red shifted from 377 to 382 nm mainly due to the addition of rGO through ZnO. The overall peak shows that the composite material of urchin-like ZnO-rGO microstructure has higher absorption capacity than pure ZnO which is confirmed from the UV-spectrum. Thus, the higher absorption capacity plays an important role in the photocatalytic performance of visible light irradiation for dyes.

To estimate the bandgap energy of synthesized catalysts, the UV-visible absorbance spectra of samples were analysed by performing by the Kubelka-Munk theory. The material was calculated by plotting $(\alpha h\nu)^2$ versus $(h\nu)$ photon energy by using the following equation:

$$\alpha h\nu = A(h\nu - Eg)^{1/2}, \tag{3}$$

where α is the absorption coefficient of the catalyst, ν is the frequency of light, $h\nu$ is the photon energy, A is the constant energy, and E_g is the bandgap energy, respectively. From Figures 4(b) and 4(c), the estimated bandgap energy values

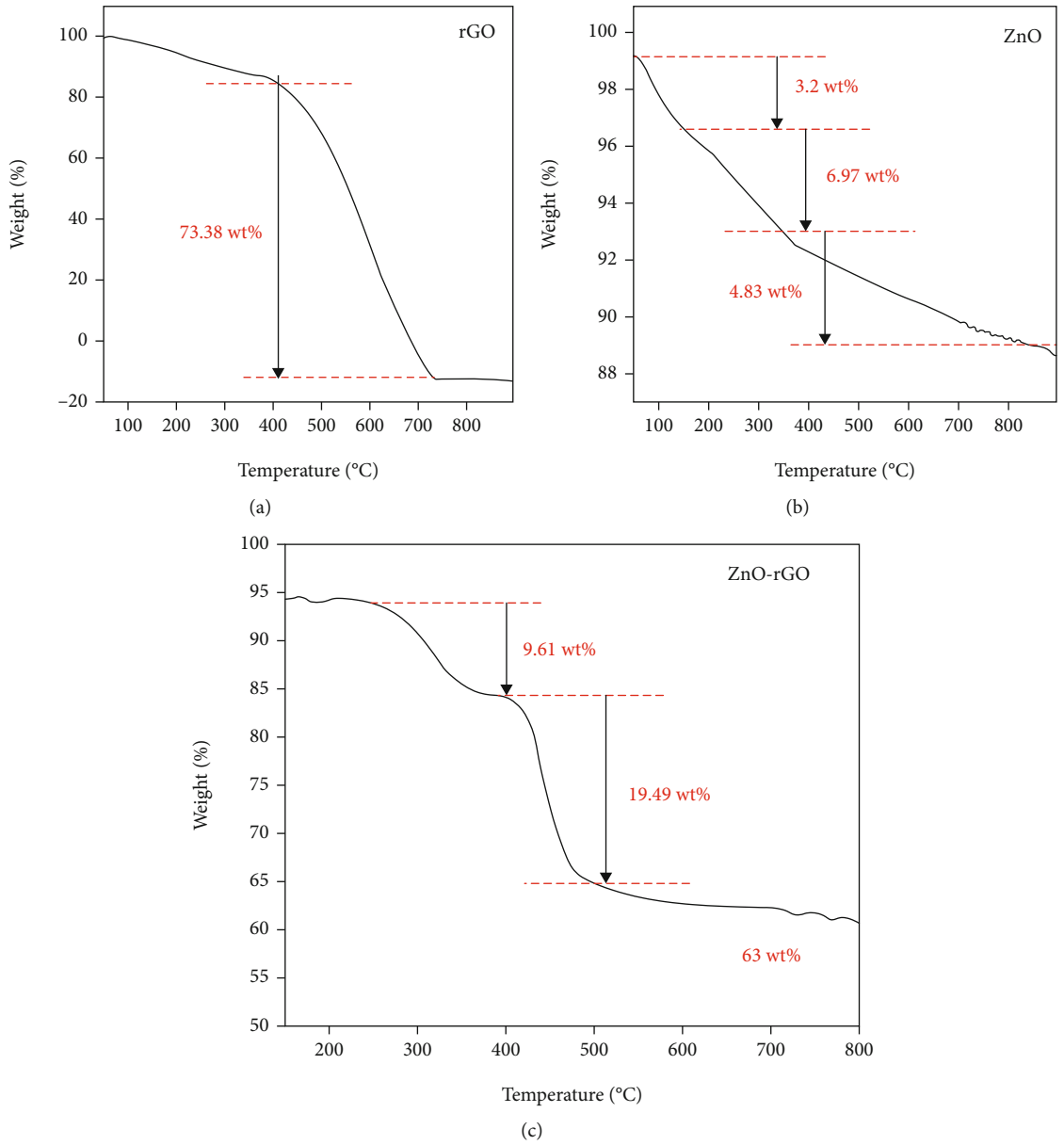

Figure 5: TGA curves of (a) rGO, (b) urchin-like ZnO, and (c) ZnO-rGO composites.

for ZnO and ZnO-rGO composites are 3.20 eV and 2.97 eV, respectively. It can be seen that the E_g value of the composite material is red shifted from the E_g value of ZnO microstructure, suggesting the bandgap reduction of ZnO-rGO catalyst, which can enhance high visible light absorption for the photocatalytic performance of phenol.

3.5. Thermogravimetric Analysis. As presented in Figure 5(a), the thermogram of rGO, the weight loss at about 73.38 wt. % mainly occurs at the range of 400°C and drops drastically due to the increasing temperature range from 410°C and 735°C, indicating that rGO has a homogeneous composition distribution to the oxidation of carbon in air simultaneously. The residual weight of rGO which is about 12.66 wt. % denotes that rGO is totally combusted [47]. From Figure 5(b), the TGA traces of ZnO one could observe the three weight loss in the range of 50-150°C, 150-350°C, and 350-600°C. Weight loss of about 3.2 wt. % from 50 to 150°C is related to the dehydration of surface-adsorbed water molecules and removal of chemically absorbed alcohol. The weight loss of about 6.97 wt. % from 150 to 350°C is due to the degradation of the organic molecules and the hydroxide groups. Therefore, annealing at above 350°C assured the formation of ZnO particles [48]. The TGA trace of ZnO-rGO composites is illustrated in Figure 5(c). The weight loss of about 9.61 wt. % above 250°C is ascribed to be oxidation of graphene under atmosphere. A significant mass loss of about 19.49 wt. % is observed at the temperature range above 400°C-510°C which is supposedly due to decomposition of rGO in the composite [49]. Based on the above result, we can conclude

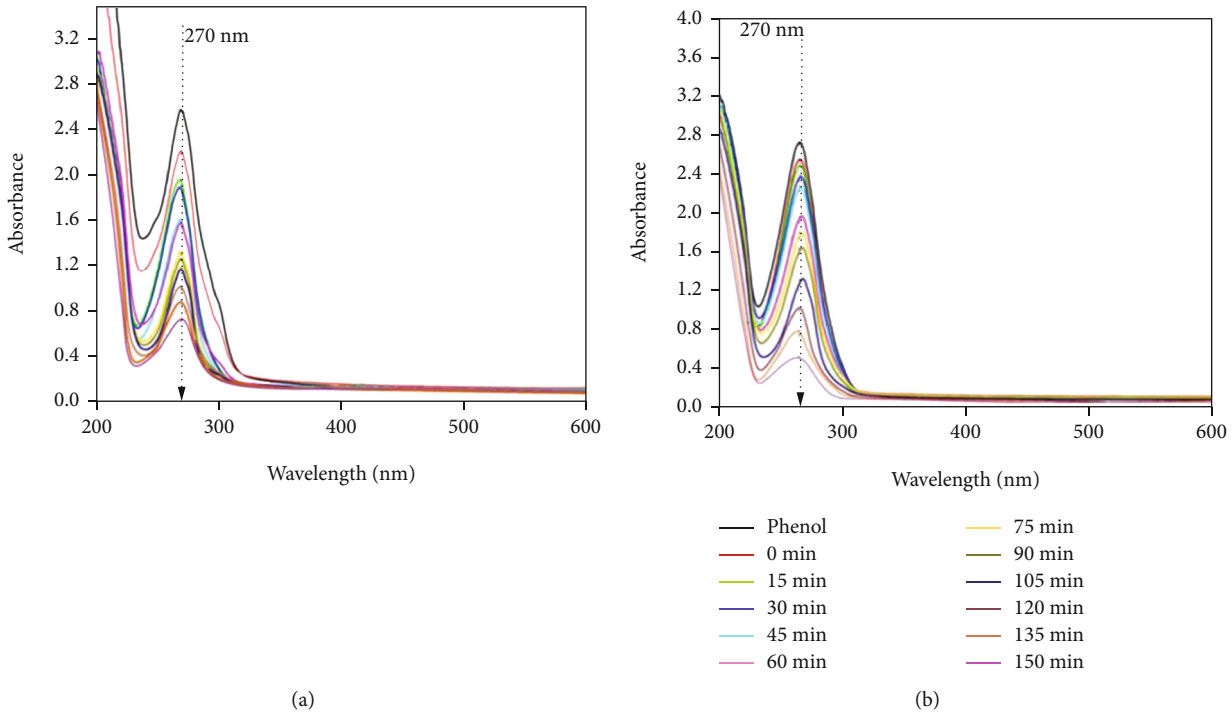

Figure 6: (a, b) UV-Vis absorption spectrum changes of phenol at every 15 min time interval of (a) urchin-like ZnO and (b) ZnO-rGO composite, respectively.

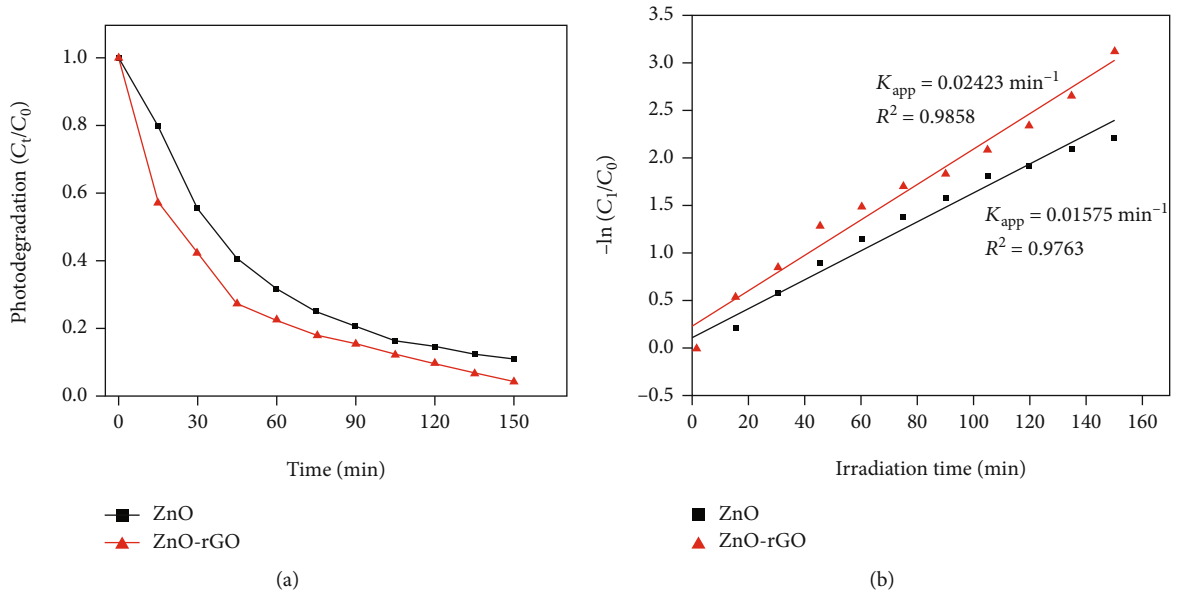

Figure 7: (a) Study of linear apparent first-order kinetics for the photodegradation of phenol solution using urchin-like ZnO and ZnO microrod-rGO catalyst under visible light illumination. (b) Photodegraded efficiencies for the ZnO-rGO nano/microcomposites and urchin-like ZnO, variation in $-\ln (C_t/C_0)$ as function of irradiation time and linear fits of photocatalysts. The kinetic rate of phenol degradation by the photocatalysts was also investigated.

that the residual weight ratio of ZnO-rGO composites is about 63 wt. % at 520°C, respectively.

3.6. Photocatalytic Activity. The photocatalytic performance of urchin-like ZnO and ZnO microrod-rGO composites was examined for their photodegradation of phenol solution as a model pollutant under visible light irradiation. Figure 6 represents the time-dependent UV-Vis absorption spectrum of the aqueous solution of phenol which leads to the decrease in its absorbance reduction with various duration. Prior to the irradiation, the sample was stirred magnetically in the completely dark area for 60 min to attain the adsorption equilibrium of phenol solution over the photocatalyst. The photodegradation was carried out for 150 min, and the

Table 1: Comparison of photocatalytic performance with previously reported literature.

Photocatalyst	Concentration ($mg\,L^{-1}$) and volume of phenol (mL)	Catalyst dosage ($g\,L^{-1}$)	Percentage of degradation (%)	Irradiation time (min)	Irradiation source	Rate constant (min^{-1})	Concentration ($mg\,L^{-1}$) and volume of phenol (mL)	Reference
$Zn/Ag_2CO_3/A\ g_2O$	50-200	0.1	1	420	Visible	—	50-200	[51]
$rGO/ZnO/TiO_2$	60-250	0.6	100	160	Visible	0.0124	60-250	[37]
Cerium doped-ZnO	20-100	1	80.7	300	Visible	0.0061	20-100	[52]
Nano ZnO500	10-100	2.5	72	60	UV-laser	0.0391	-100	[53]
Fe_3O_4-ZnO	10-200	0.32	82.3	150	UV	0.0108	-200	[20]
Aqueous ZnO	70-100	2.5	100	480	Sunlight	0.325	70-100	[30]
ZnO	50-500	0.6	100	360	Solar	$0.3954 \pm 0.008\,h^{-1}$	50-500	[1]
TiO_2/rGO-8%	20-100	—	58.8	720	Visible	$0.0014\,h^{-1}$	20-100	[54]
ZnO nanorods	10	—	50	300	Visible	—	10	[55]
Urchin-like ZnO microrod-rGO	20-50	0.2	84.2	150	Visible	0.02423	20-50	This work

degradation rate of phenol solution has shown a maximum absorption wavelength at $\lambda_{max} = 270$ nm [3].

In general, the concentration of phenol or absorbance gradually decreases with the increasing illumination time in the presence of urchin-like ZnO and ZnO-rGO photocatalyst, respectively. After irradiation, the concentration of phenol is reduced, implying the decolourization of photocatalyst, and ascribed to the oxidation of phenol in the existence of –OH radicals. The degradation result shows that the ZnO nano/micro-rGO heterojunction degrades the organic pollutants of phenol solution up to ~84.2% and urchin-like ZnO catalyst degrades ~71.5% in just 150 min under similar operating conditions. Therefore, the ZnO nano/microrod-rGO composites exhibit better photocatalytic activity than those of urchin-like ZnO microrods. As shown in Figures 6(a) and 6(b), the typical absorption peak at 270 nm does not change its wavelength even after 150 min, which indicated that the prepared photocatalyst of phenol is active under visible light irradiation.

According to literature, the addition of rGO in the catalysts favours a larger surface area to bind a phenol molecule through the $\pi - \pi$ conjugation with face-to-face direction [50]. The dispersion of ZnO-rGO composites enhances the surface of oxygen species, improves the electron-hole pairs, and lowers the bandgap. Moreover, the absorption edge of ZnO-rGO composites shifted to the broad wavelength after 135 min and provides a favourable absorption of phenol under visible light irradiation. The observed normalized temporal concentration changes (C_t/C_0) of phenol during photodegradation activity of prepared photocatalysts (urchin-like ZnO and ZnO microrod-rGO composites) vs. time graph are shown in Figure 7(a). It is clear that ZnO-rGO with 84.2% demonstrates an outstanding enhancement in the photodegradation of phenol compared with urchin-like ZnO microrods.

Pseudo-first-order reaction. The reaction was calculated from the slope of $-\ln(C_t/C_0)$ and reaction time, t (Figure 7(b)). From this graph, we can understand that urchin-like ZnO and ZnO microrod-rGO composites exhibit linear fit lines and confirm that the photocatalytic degradation reaction follows pseudo-first-order reaction kinetics. As shown in Figure 7(b), the rate constant of urchin-like ZnO exhibits a K_{app} of $0.015\,min^{-1}$, whereas the ZnO microrod-rGO composites reach into $0.024\,min^{-1}$, which is about 1.5 times faster rate than that of pure ZnO microrods. The higher rate constant of ZnO microrod-rGO composites yields a large number of photoelectrons which enhance the photocatalysis. Herein, to better assess, the performance of the synthesized catalyst was compared with the detoxification of phenol reported in literature studies (Table 1). It is concluded that ZnO microrod-rGO composites are an efficient catalyst for decontamination of phenol over visible light irradiation. It may be beneficial for the use of industrial applications due to its cost-effective and great performance.

4. Conclusion

In this investigation, we successfully synthesized a cost-effective and highly active ZnO microrod-rGO composite of heterojunction via a facile hydrothermal process. The ZnO-rGO (2.97 eV) displayed a narrow bandgap when compared to urchin-like ZnO (3.20 eV) and also showed strong visible light absorption and an enhanced photoresponse to visible light regions. The photodegradation efficiency of the composite reached 84.2%, and the catalyst performance was evaluated by phenol degradation under the irradiation of visible light. The ZnO-rGO composite incorporated with additional electronic channels with the presence of urchin-like structure can absorb a large quantity of phenol because of its large surface area and transfer of electrons faster due to the presence of rGO in the composite. Therefore, the obtained results suggest that the prepared ZnO-rGO composite is a promising candidate for photodegradation process under visible-light-driven photocatalyst for decontamination of toxic compounds and effluents.

Data Availability

The data supporting this work is available from the corresponding author upon request.

Conflicts of Interest

The authors declare that they have no conflicts of interest.

Supplementary Materials

The pictorial representation of this work has been described in the form of graphical abstract available in the supplementary information. *(Supplementary Materials)*

References

[1] N. Yusoff, S.-A. Ong, L.-N. Ho, Y.-S. Wong, and W. Khalik, "Degradation of phenol through solar-photocatalytic treatment by zinc oxide in aqueous solution," *Desalination and Water Treatment*, vol. 54, pp. 1621–1628, 2014.

[2] N. C. Saha, F. Bhunia, and A. Kaviraj, "Toxicity of phenol to fish and aquatic ecosystems," *Bulletin of Environmental Contamination and Toxicology*, vol. 63, no. 2, pp. 195–202, 1999.

[3] F. Hayati, A. A. Isari, M. Fattahi, B. Anvaripour, and S. Jorfi, "Photocatalytic decontamination of phenol and petrochemical wastewater through ZnO/TiO_2 decorated on reduced graphene oxide nanocomposite: influential operating factors, mechanism, and electrical energy consumption," *RSC Advances*, vol. 8, no. 70, pp. 40035–40053, 2018.

[4] A. Lakshmanan, P. Surendran, S. SakthyPriya et al., "Effect of fuel content on nonlinear optical and antibacterial activities of $Zn/Cu/Al_2O_4$ nanoparticles prepared by microwave-assisted combustion method," *Journal of King Saud University - Science*, vol. 32, no. 2, pp. 1382–1389, 2020.

[5] M. Ahmad, E. Ahmed, Z. L. Hong, W. Ahmed, A. Elhissi, and N. R. Khalid, "Photocatalytic, sonocatalytic and sonophotocatalytic degradation of rhodamine B using ZnO/CNTs composites photocatalysts," *Ultrasonics Sonochemistry*, vol. 21, no. 2, pp. 761–773, 2014.

[6] S. Fang, K. Lv, Q. Li, H. Ye, D. Du, and M. Li, "Effect of acid on the photocatalytic degradation of rhodamine B over g-C_3N_4," *Applied Surface Science*, vol. 358, pp. 336–342, 2015.

[7] X. Wang, J. Wang, P. Guo, W. Guo, and C. Wang, "Degradation of rhodamine B in aqueous solution by using swirling jet-induced cavitation combined with H_2O_2," *Journal of Hazardous Materials*, vol. 30, pp. 486–491, 2009.

[8] S. Ravichandran and G. Ramalingam, "Synthesis, optical and morphological studies of sol-gel derived ZnO/PVP one dimensional nano-composite," *Journal of Nanoscience and Nanotechnology*, vol. 1, pp. 39–43, 2013.

[9] K. Mishra and P. Gogate, "Intensification of degradation of rhodamine B using hydrodynamic cavitation in the presence of additives," *Separation and Purification Technology*, vol. 75, no. 3, pp. 385–391, 2010.

[10] I. Oller, S. Malato, and J. A. Sánchez-Pérez, "Combination of advanced oxidation processes and biological treatments for wastewater decontamination—a review," *Science of The Total Environment*, vol. 409, no. 20, pp. 4141–4166, 2011.

[11] G. Theophil Anand, D. Renuka, R. Ramesh et al., "Green synthesis of ZnO nanoparticle using Prunus dulcis (almond gum) for antimicrobial and supercapacitor applications," *Surfaces and Interfaces*, vol. 17, p. 100376, 2019.

[12] M. Antonopoulou, E. Evgenidou, D. Lambropoulou, and I. Konstantinou, "A review on advanced oxidation processes for the removal of taste and odor compounds from aqueous media," *Water Research*, vol. 53, pp. 215–234, 2014.

[13] M. R. S. Joice, T. M. David, and P. Wilson, "WO3 nanorods supported on mesoporous TiO_2 nanotubes as one-dimensional nanocomposites for rapid degradation of methylene blue under visible light irradiation," *Journal of Physical Chemistry C*, vol. 123, no. 45, pp. 27448–27464, 2019.

[14] H. Huang, H. Ouyang, T. Han, H. Wang, and X. Zheng, "Construction of carbon quantum dots/single crystal TiO_2 nanosheets with exposed {001} and {101} facets and their visible light driven catalytic activity," *RSC Advances*, vol. 9, no. 7, pp. 3532–3541, 2019.

[15] S. G. Kumar and L. G. Devi, "Review on modified TiO_2 photocatalysis under UV/visible light: selected results and related mechanisms on interfacial charge carrier transfer dynamics," *The Journal of Physical Chemistry. A*, vol. 115, no. 46, pp. 13211–13241, 2011.

[16] G. Ramalingam, C. Ragupathi, K. Kaviyarasu et al., "Up-scalable synthesis of size-controlled white-green emitting behavior of core/shell (CdSe/ZnS) quantum dots for LED applications," *Journal of Nanoscience and Nanotechnology*, vol. 19, no. 7, pp. 4026–4032, 2019.

[17] A. L. Linsebigler, G. Lu, and J. T. Yates, "Photocatalysis on TiO_2 surfaces: principles, mechanisms, and selected results," *Chemical Reviews*, vol. 95, no. 3, pp. 735–758, 1995.

[18] S. Anas, S. Rahul, K. B. Babitha, R. V. Mangalaraja, and S. Ananthakumar, "Microwave accelerated synthesis of zinc oxide nanoplates and their enhanced photocatalytic activity under UV and solar illuminations," *Applied Surface Science*, vol. 355, pp. 98–103, 2015.

[19] H. Yin, K. Yu, C. Song, R. Huang, and Z. Zhu, "Synthesis of Au-decorated V2O5@ZnO heteronanostructures and enhanced plasmonic photocatalytic activity," *ACS Applied Materials & Interfaces*, vol. 6, no. 17, pp. 14851–14860, 2014.

[20] X. Feng, H. Guo, K. Patel, H. Zhou, and X. Lou, "High performance, recoverable Fe_3O_4ZnO nanoparticles for enhanced photocatalytic degradation of phenol," *Chemical Engineering Journal*, vol. 244, pp. 327–334, 2014.

[21] S. Jorfi, G. Barzegar, M. Ahmadi et al., "Enhanced coagulation-photocatalytic treatment of acid red 73 dye and real textile wastewater using UVA/synthesized MgO nanoparticles," *Journal of Environmental Management*, vol. 15, pp. 111–118, 2016.

[22] P. S. Chauhan, R. Kant, A. Rai, A. Gupta, and S. Bhattacharya, "Facile synthesis of ZnO/GO nanoflowers over Si substrate for improved photocatalytic decolorization of MB dye and industrial wastewater under solar irradiation," *Materials Science in Semiconductor Processing*, vol. 89, pp. 6–17, 2019.

[23] A. Meng, J. Shao, X. Fan, J. Wang, and Z. Li, "Rapid synthesis of a flower-like ZnO/rGO/Ag micro/nano-composite with enhanced photocatalytic performance by a one-step microwave method," *RSC Advances*, vol. 4, no. 104, pp. 60300–60305, 2014.

[24] P. Van Tuan, T. T. Phuong, V. T. Tan, S. X. Nguyen, and T. N. Khiem, "In-situ hydrothermal fabrication and photocatalytic behavior of ZnO/reduced graphene oxide nanocomposites with varying graphene oxide concentrations," *Materials Science in Semiconductor Processing*, vol. 115, p. 105114, 2020.

[25] V. A. Tu and V. A. Tuan, "A facile and fast solution chemistry synthesis of porous ZnO nanoparticles for high efficiency photodegradation of tartrazine," *Vietnam Journal of Chemistry*, vol. 56, no. 2, pp. 214–219, 2018.

[26] T. H. Le, Q. D. Truong, T. Kimura et al., "Synthesis of hierarchical porous ZnO microspheres and its photocatalytic deNOx activity," *Ceramics International*, vol. 38, no. 6, pp. 5053–5059, 2012.

[27] M. Darvishi, F. Jamali-Paghaleh, M. Jamali-Paghaleh, and J. Seyed-Yazdi, "Facile synthesis of ZnO/rGO hybrid by microwave irradiation method with improved photoactivity," *Surfaces and Interfaces*, vol. 9, pp. 167–172, 2017.

[28] K. Huang, Y. H. Li, S. Lin et al., "A facile route to reduced graphene oxide-zinc oxide nanorod composites with enhanced photocatalytic activity," *Powder Technology*, vol. 257, pp. 113–119, 2014.

[29] S. Xu, L. Fu, T. S. H. Pham, A. Yu, F. Han, and L. Chen, "Preparation of ZnO flower/reduced graphene oxide composite with enhanced photocatalytic performance under sunlight," *Ceramics International*, vol. 41, no. 3, pp. 4007–4013, 2015.

[30] S. K. Pardeshi and A. B. Patil, "A simple route for photocatalytic degradation of phenol in aqueous zinc oxide suspension using solar energy," *Solar Energy*, vol. 82, no. 8, pp. 700–705, 2008.

[31] J. Qin, X. Zhang, C. Yang, M. Cao, M. Ma, and R. Liu, "ZnO microspheres-reduced graphene oxide nanocomposite for photocatalytic degradation of methylene blue dye," *Applied Surface Science*, vol. 392, pp. 196–203, 2017.

[32] H. R. Pant, C. H. Park, P. Pokharel, L. D. Tijing, D. S. Lee, and C. S. Kim, "ZnO micro-flowers assembled on reduced graphene sheets with high photocatalytic activity for removal of pollutants," *Powder Technology*, vol. 235, pp. 853–858, 2013.

[33] N. Cao and Y. Zhang, "Study of reduced graphene oxide preparation by hummers' method and related characterization," *Journal of Nanomaterials*, vol. 2015, Article ID 168125, 5 pages, 2015.

[34] E. Andrijanto, S. Shoelarta, G. Subiyanto, and S. Rifki, "Facile synthesis of graphene from graphite using ascorbic acid as reducing agent," *AIP Conference Proceedings*, vol. 1725, p. 20003, 2016.

[35] Y. Feng, N. Feng, Y. Wei, and G. Zhang, "An in situ gelatin-assisted hydrothermal synthesis of ZnO–reduced graphene

oxide composites with enhanced photocatalytic performance under ultraviolet and visible light," *RSC Advances*, vol. 4, no. 16, pp. 7933–7943, 2014.

[36] M. Pusty, A. K. Rana, Y. Kumar, V. Sathe, S. Sen, and P. Shirage, "Synthesis of partially reduced graphene oxide/silver nanocomposite and its inhibitive action on pathogenic fungi grown under ambient conditions," *ChemistrySelect*, vol. 1, no. 14, pp. 4235–4245, 2016.

[37] H. Moussa, E. Girot, K. Mozet, H. Alem, G. Medjahdi, and R. Schneider, "ZnO rods/reduced graphene oxide composites prepared _via_ a solvothermal reaction for efficient sunlight-driven photocatalysis," *Applied Catalysis B: Environmental*, vol. 185, pp. 11–21, 2016.

[38] H.-W. Wang, Z.-A. Hu, Y.-Q. Chang et al., "Design and synthesis of $NiCo_2O_4$–reduced graphene oxide composites for high performance supercapacitors," *Journal of Materials Chemistry*, vol. 21, no. 28, pp. 10504–10511, 2011.

[39] Y. Zhou, D. Li, L. Yang et al., "Preparation of 3D urchin-like RGO/ZnO and its photocatalytic activity," *Journal of Materials Science: Materials in Electronics*, vol. 28, no. 11, pp. 7935–7942, 2017.

[40] H. N. Tien, V. H. Luan, L. T. Hoa et al., "One-pot synthesis of a reduced graphene oxide-zinc oxide sphere composite and its use as a visible light photocatalyst," *Chemical Engineering Journal*, vol. 229, pp. 126–133, 2013.

[41] L. Zhang, L. Du, X. Cai et al., "Role of graphene in great enhancement of photocatalytic activity of ZnO nanoparticle-graphene hybrids," *Physica E: Low-dimensional Systems and Nanostructures*, vol. 47, pp. 279–284, 2013.

[42] D. Gnanasangeetha and D. Saralathambavani, "One pot synthesis of zinc oxide nanoparticles via chemical and green method," *Research Journal of Material Sciences*, vol. 1, pp. 1–8, 2013.

[43] K. Rokesh, A. Nithya, K. Jeganathan, and K. Jothivenkatachalam, "A facile solid state synthesis of cone-like ZnO microstructure an efficient solar-light driven photocatalyst for rhodamine B degradation," *Materials Today: Proceedings*, vol. 3, no. 10, pp. 4163–4172, 2016.

[44] Q.-P. Luo, X.-Y. Yu, B.-X. Lei, H.-Y. Chen, D.-B. Kuang, and C.-Y. Su, "Reduced graphene oxide-hierarchical ZnO hollow sphere composites with enhanced photocurrent and photocatalytic activity," *Journal of Physical Chemistry C*, vol. 116, no. 14, pp. 8111–8117, 2012.

[45] Q. Zhang, C. Tian, A. Wu et al., "A facile one-pot route for the controllable growth of small sized and well-dispersed ZnO particles on GO-derived graphene," *Journal of Materials Chemistry*, vol. 22, no. 23, pp. 11778–11784, 2012.

[46] H.-B. Kim, D.-W. Jeong, and D.-J. Jang, "Morphology-tunable synthesis of ZnO microstructures under microwave irradiation: formation mechanisms and photocatalytic activity," *CrystEngComm*, vol. 18, no. 6, pp. 898–906, 2016.

[47] P. Liu, Y. Huang, and X. Zhang, "Cubic $NiFe_2O_4$ particles on graphene-polyaniline and their enhanced microwave absorption properties," *Composites Science and Technology*, vol. 107, pp. 54–60, 2015.

[48] J. Wang, G. Wang, S. Miao, J. Li, and X. Bao, "Graphene-supported iron-based nanoparticles encapsulated in nitrogen-doped carbon as a synergistic catalyst for hydrogen evolution and oxygen reduction reactions," *Faraday Discussions*, vol. 176, pp. 135–151, 2014.

[49] F. B. Dejene, A. G. Ali, H. C. Swart et al., "Optical properties of ZnO nanoparticles synthesized by varying the sodium hydroxide to zinc acetate molar ratios using a sol-gel process," *Central European Journal of Physics*, vol. 9, no. 5, pp. 1321–1326, 2011.

[50] X. Zhou, T. Shi, and H. Zhou, "Hydrothermal preparation of ZnO-reduced graphene oxide hybrid with high performance in photocatalytic degradation," *Applied Surface Science*, vol. 258, no. 17, pp. 6204–6211, 2012.

[51] N. Rosman, W. N. W. Salleh, A. F. Ismail et al., "Photocatalytic degradation of phenol over visible light active $ZnO/Ag_2CO_3/Ag_2O$ nanocomposites heterojunction," *Journal of Photochemistry and Photobiology A: Chemistry*, vol. 364, pp. 602–612, 2018.

[52] J.-C. Sin, S.-M. Lam, K.-T. Lee, and A. R. Mohamed, "Preparation of cerium-doped ZnO hierarchical micro/nanospheres with enhanced photocatalytic performance for phenol degradation under visible light," *Journal of Molecular Catalysis A: Chemical*, vol. 409, pp. 1–10, 2015.

[53] K. Hayat, M. A. Gondal, M. M. Khaled, S. Ahmed, and A. M. Shemsi, "Nano ZnO synthesis by modified sol gel method and its application in heterogeneous photocatalytic removal of phenol from water," *Applied Catalysis A: General*, vol. 393, no. 1-2, pp. 122–129, 2011.

[54] G. Wang, W. Guo, D. Xu, D. Liu, and M. Qin, "Graphene oxide hybridised TiO_2 for visible light photocatalytic degradation of phenol," *Symmetry (Basel)*, vol. 12, no. 9, article ???, 2020.

[55] J. Al-Sabahi, T. Bora, M. Al-Abri, and J. Dutta, "Controlled defects of zinc oxide nanorods for efficient visible light photocatalytic degradation of phenol," *Materials (Basel)*, vol. 9, no. 4, p. 238, 2016.

Hindawi
Journal of Nanomaterials
Volume 2021, Article ID 5576048, 11 pages
https://doi.org/10.1155/2021/5576048

Research Article

Facile Synthesis of rGO/Mn_3O_4 Composite for Efficient Photodegradation of Phenol under Visible Light

P. Shobha,[1] Albin John P. Paul Winston,[1] S. Sunil,[1] T. Manovah David,[2] S. Mary Margaret,[1] S. Muthupandi,[1] and P. Sagayaraj[1]

[1]*Department of Physics, Loyola College (Autonomous), Chennai 34, India*
[2]*Thin Films and Coatings Section, Materials Science Group, Indira Gandhi Centre for Atomic Research, Kalpakkam 603 102, India*

Correspondence should be addressed to P. Sagayaraj; sagayaraj1962@gmail.com

Received 20 January 2021; Revised 16 March 2021; Accepted 18 April 2021; Published 7 June 2021

Academic Editor: G. Ravi

To enhance reusability and to maintain higher efficiency in degradation, Mn_3O_4/rGO nanocomposites were synthesized by a facile thermal treatment. Initially, Mn_3O_4 nanoparticles were prepared and analyzed by powder XRD and HR-SEM. The composition of manganese oxide was varied to obtain different nanocomposites. The Mn_3O_4 ions were found to be well anchored onto the rGO surface. The obtained samples were taken for the photodegradation studies with phenol as the pollutant. Under a dynamic mode, the absorption efficiency was found to be maximum for the MnsR0.75 sample for phenol.

1. Introduction

Discharge of organic wastes into local water bodies has been one of the most serious issues. The highly toxic wastes in industrial effluents contain a large portion of phenolic compounds that have adverse effects on both nature and public health [1–3]. The common sources of phenolic pollution are paints, pesticides, coke ovens, coal conversion, polymeric resin, paper mills, petroleum refineries, and petrochemical and pharmaceutical industries [4–6]. These compounds have stubborn nonbiodegradable properties and toxicity and, therefore, posed to be fatally harmful to aquatic life and humans since the phenolic compounds own considerably high binding capacity in aqueous medium. Furthermore, their unpleasant odor and taste add to the detrimental effect on aqueous systems [7–10]. Thus, it is important to develop an adhesive-like material to remove the organic pollutants from water bodies to minimize pollution [11–13]. Many techniques have been used to remove phenol from wastewater such as photocatalytic degradation, membrane filtration, chemical oxidation, and solvent extraction [14–21]. Recently, Wang et al. prepared 2D/2D γ-MnO_2/rGO using rGO and $KMnO_4$ for the catalytic ozonation of 4-chlorophenol in the presence of PMS [22]. Ramesh et al. examined the catalytic efficiency of MnO_2/rGO nanowires for the degradation of reactive red using a sono-Fenton-assisted process in the presence of H_2O_2 [23]. Qu et al. used a suspension of GO/$MnSO_4$ from the modified Hummers method to fabricate rGO/MnO_2 to degrade methylene blue dye in the presence of H_2O_2 [24]. Recently, the research has turned towards the removal of pollutants via photocatalysis employing either UV or visible light [25–29]. In recent times, rGO has gained considerable attention in this area as an effective metal-free catalyst which has been used in order to weaken up the persulphate, eventually wearing away the O-O band present at the dynamic sites and forming an excellent electron bridge (Duan et al., 2015, [30]). In a similar way, nanodiamonds, cubic mesoporous carbon, and CNT have been extensively used by researchers in degrading organic pollutants [2, 31, 32]. Though these materials caused degradation of the target compounds, a longer time was required to achieve a complete degradation. Hence, graphene was employed in this work to attain a higher surface area along with unique properties such as good conductivity, charge delocalization, chemical stability, and electron transfer properties thereby making it an excellent candidate for the purpose. Graphene, with these qualities, could be considered a suitable material to be used in the degradation of organic pollutants [26, 33]. In addition,

metal oxides based on manganese have been extensively explored owing to their superior physical and chemical properties, low toxicity, and abundance. The presence of their unique redox loops leads to a higher potential activity via the single electron transfer making its way to be a suitable catalyst [34]. The additional difficulty arises due to the superfine nature of Mn as it forms a well-dispersed solution [35, 36]. In a nutshell, photocatalysis is the acceleration of photoelectrons due to the presence of a catalyst like Mn used in this case. Thus, more attention has been paid towards metal-free catalysts like carbon materials which are both cheap and environment-friendly and also for sustainable sources. In a typical heterogeneous experiment, the carbon material will be acting as an adsorbent [37], catalytic support [38], and in some cases also a catalytic support [39]. These peculiar properties make it an interesting candidate along with other properties like their stability with acids and bases, surface, texture, and mechanical and electrical properties. It is also commendable to observe that the incorporation of a carbon material induces an encouraging effect not only on the efficiency but also on the degree of degradation achieved in the reactions [40, 41]. This work is aimed at creating a metal oxide-based composite with the addition of a carbon support to facilitate a better degradation of phenol.

2. Materials and Methods

2.1. Synthesis of rGO. All the chemicals used were of analytical grade and used without any further purification. In a synthesis procedure, 1 g of graphite flakes was added to 50 ml concentrated sulfuric acid while stirring in an ice-water bath and maintaining the temperature under 10°C. 0.379 M potassium permanganate was gradually added to the above solution; the reaction was quenched by the addition of 200 ml distilled water. An extra 2 h ultrasonic treatment was carried out and processed for the preparation (reduction) of rGO. After adjusting the pH to ~6 with the addition of sodium hydroxide (0.1 M), the suspension was further sonicated for 1 h. 0.567 M of the reducing agent L-ascorbic acid was dissolved in 100 ml distilled water and then was slowly added to the exfoliated graphite oxide suspension at room temperature, to act as a mild reducing agent. The reduction was performed by maintaining the solution at 95°C for 1 h. The resultant black precipitate was simply filtered by cellulose filter paper and was further washed with a 1 M hydrochloric acid solution to wash away the remaining impurities and followed by washes in distilled water, and the pH was brought to neutral. Finally, the filtrate was freeze-dried to obtain rGO powder.

2.2. Synthesis of Mn_3O_4 Nanospheres. The sol-process is one of the easiest ways to synthesize Mn_3O_4 nanostructures. An aqueous solution consisting of manganous chloride (0.05 M) and N,N-dimethylformamide (0.01 M) was stirred on a magnetic stirrer at room temperature for 15 min. Under this stirring condition, an equal volume of 0.05 M sodium hydroxide was added drop-wise into this reaction mixture. The colorless solution turns initially to light brown and later to a dark brown colloidal precipitate, which indicates the formation of

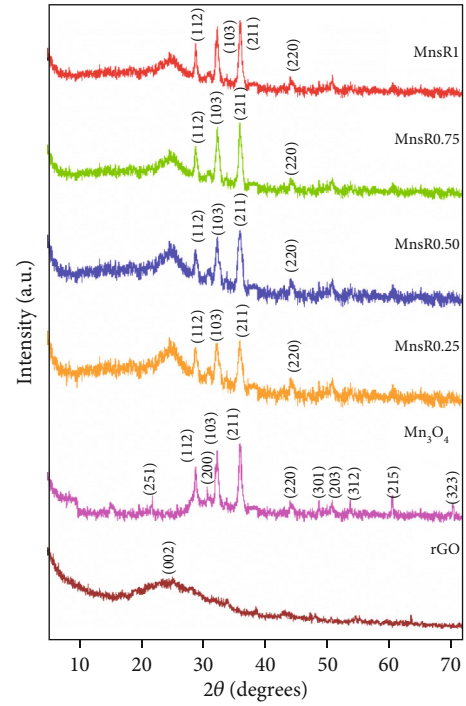

Figure 1: X-ray diffractograms of rGO, pristine Mn_3O_4, MnsR0.25, MnsR0.50, MnsR0.75, and MnsR1.

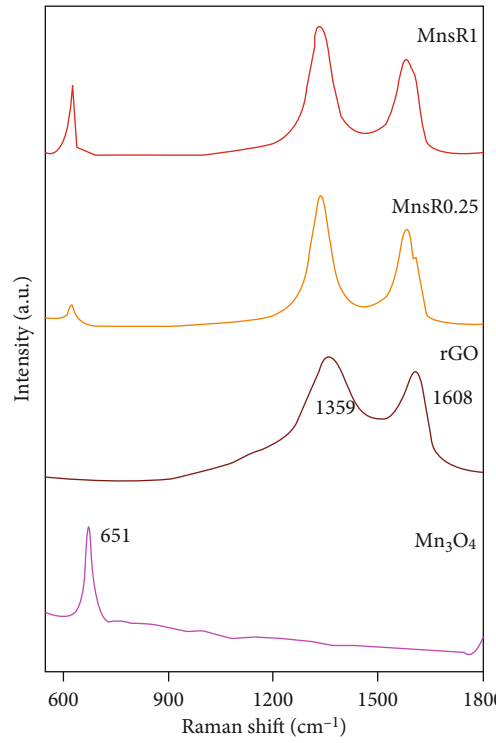

Figure 2: Raman plot of pristine Mn_3O_4, rGO, MnsR0.25, and MnsR1.

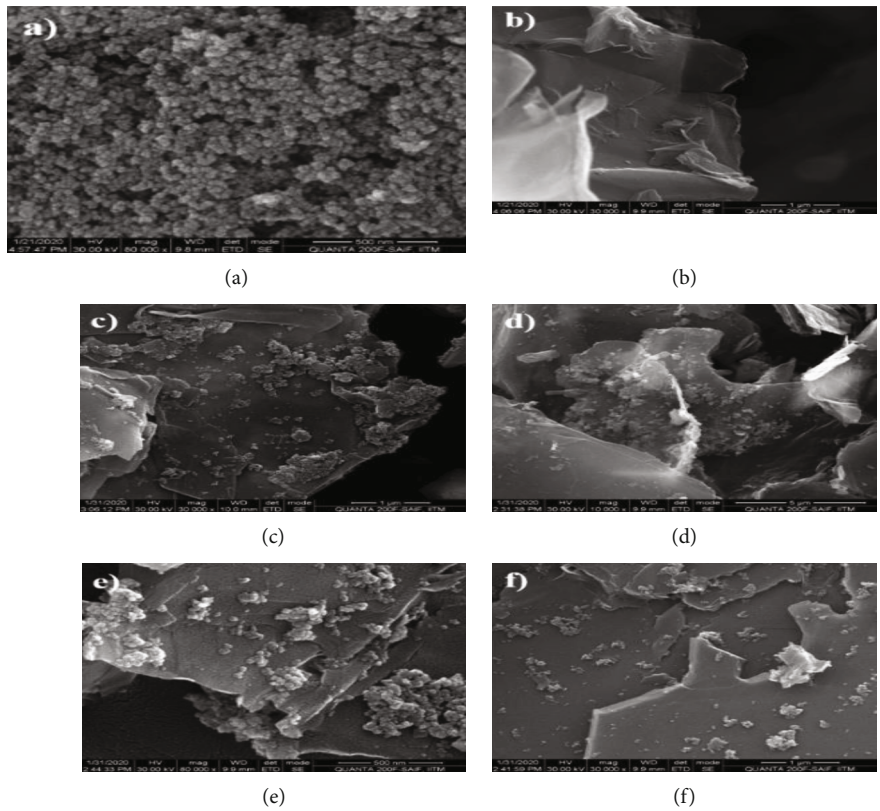

FIGURE 3: HR-SEM images of (a) pristine Mn_3O_4, (b) bare rGO, (c) MnsR1, (d) MnsR0.75, (e) MnsR0.50, and (f) MnsR0.25.

the Mn_3O_4 nanostructure. The stirring process was prolonged for 2 hours. The particles were centrifuged and washed with distilled water several times and finally with ethanol and then conventionally annealed at 400°C for 2 hours to eliminate the coordinated H_2O molecule.

2.3. Preparation of rGO/Mn_3O_4 Nanocomposites. The rGO/Mn_3O_4 nanocomposites were formed from the individually prepared rGO and Mn_3O_4 nanoparticles. Ethylene glycol aided in the composite formation process; 100 mg of Mn_3O_4 was added to 20 ml of ethylene glycol and then for an hour. A brownish-black color solution was obtained, and to this colloidal solution, an equal amount (100 mg) of rGO was added. The colloidal mixture was allowed to stir for 30 minutes and dried in an oven at 140°C to obtain the rGO/Mn_3O_4 composites. By keeping the mass of rGO a constant (100 mg), three more composites were prepared by changing the Mn_3O_4 mass as 25, 50, and 75 mg. The samples prepared with the mass of 25, 50, 75, and 100 mg are labeled as MnsR0.25, MnsR0.50, MnsR0.75, and MnsR1, respectively.

2.4. Characterization. The structural, morphological, optical, compositional, and thermal data of the as-prepared samples were investigated. X-ray diffraction was carried out on a Rich Seifert X-ray diffractometer in the range 10-75°; Raman analysis was performed with the QE Pro Raman Series Spectrometer. HR-SEM and EDX analyses were carried out on a Quanta 200 FEG High-Resolution Scanning Electron Microscope equipped with an EDAX analyzer. The FT-IR spectrum was taken on Perkin Elmer Spectrum Two within a range of 500-4000 cm^{-1}. TG thermograms were obtained from Perkin Elmer STA 6000 in the presence of nitrogen atmosphere (20 ml/hr) in the temperature range of 100-800°C.

3. Results and Discussion

Figure 1 shows the X-ray diffraction (XRD) pattern of the synthesized rGO sheets which exhibits a broad diffraction peak at 24°. The powder XRD pattern of the as-prepared Mn_3O_4 is depicted in Figure 1. These peaks were conveniently indexed to a pure tetragonal phase of the Mn_3O_4 nanostructure (JCPDS card No. 89-4837) [41]. The peaks of the composite indicate the presence of Mn_3O_4; the steady increase in the intensity of the peaks indicates the increasing presence of manganese in the composites from MnsR0.25 to MnsR1. The same has been reflected in the Raman analysis depicted in Figure 2. The XRD pattern of rGO/Mn_3O_4 nanocomposites is shown in Figure 1, and it shows no structural changes and contains perfect combinations of the above peaks corresponding to both Mn_3O_4 and rGO. The crystallite size of Mn_3O_4 nanospheres was calculated by the Debye-Scherrer formula:

$$D = \frac{k\lambda}{\beta \cos \theta}, \quad (1)$$

where D is the crystalline size, k is the shape factor, λ is the wavelength of X-ray, β is the full-width half maxima of the peak, and θ the angle at which the peak has been observed. The particle size of the Mn_3O_4 nanosphere is calculated to

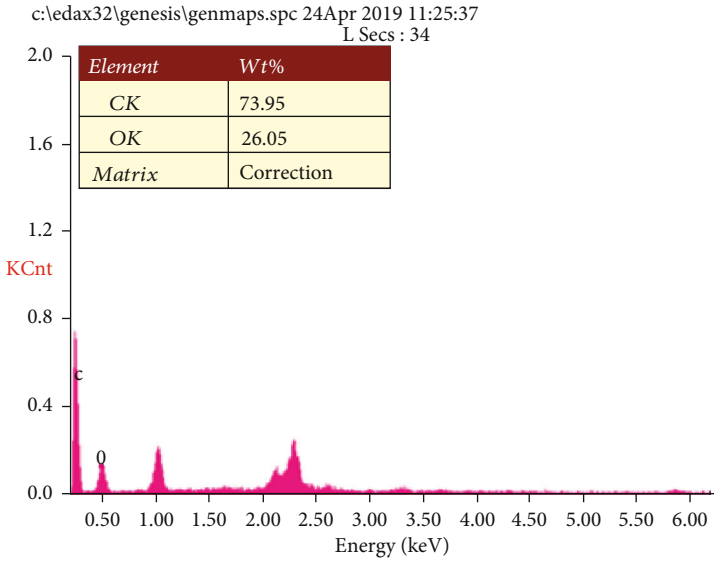

(a)

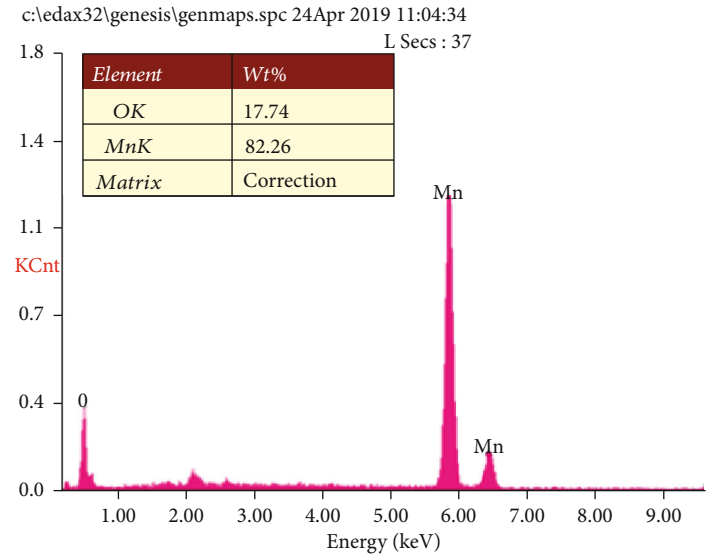

(b)

Figure 4: Continued.

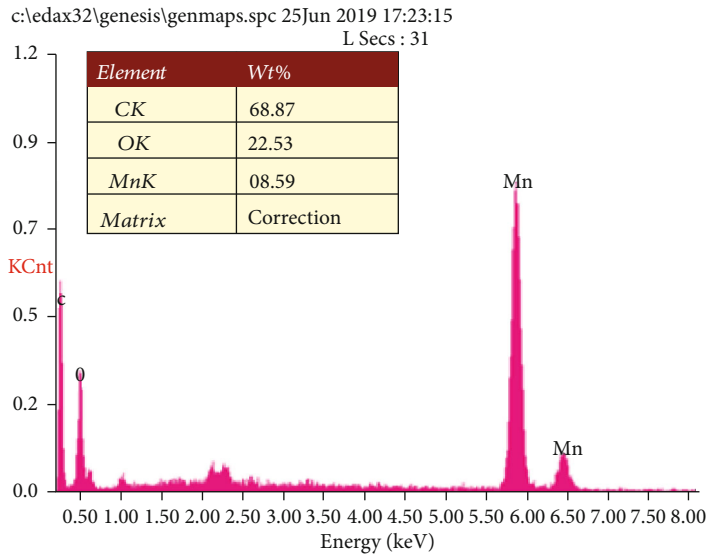

(c)

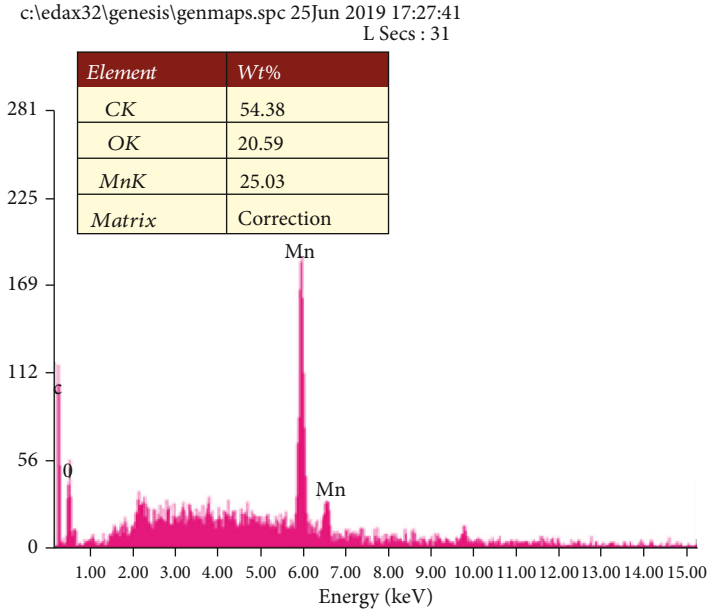

(d)

Figure 4: Continued.

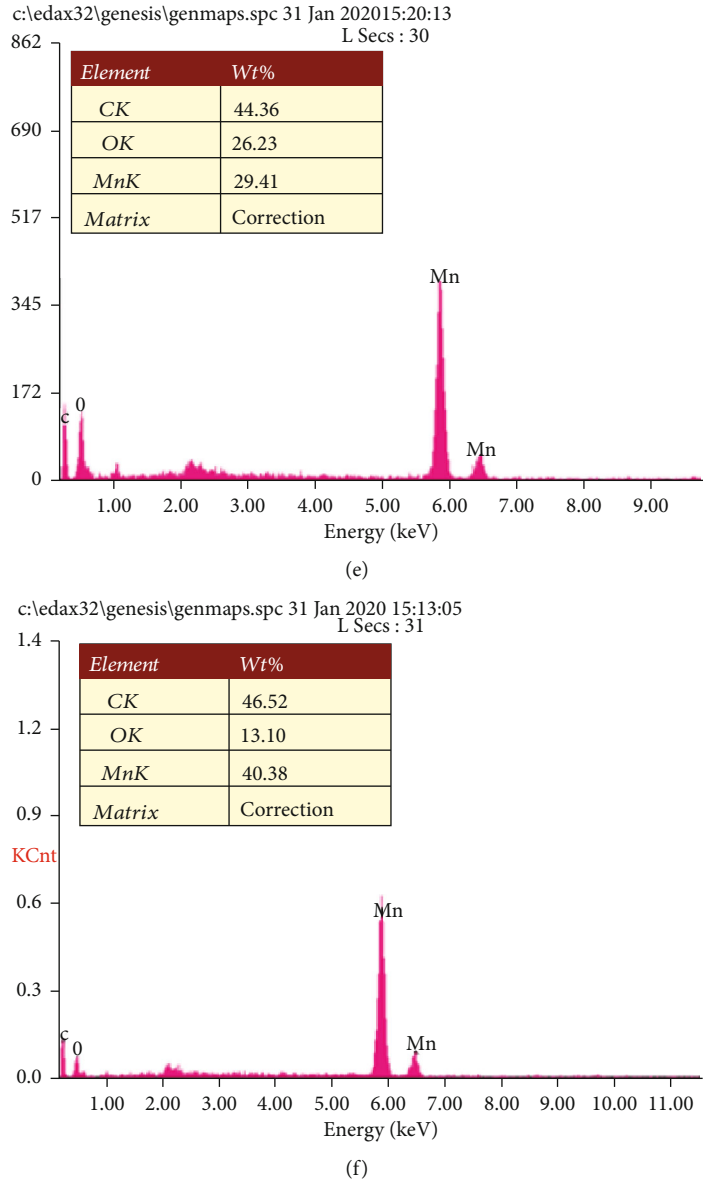

Figure 4: EDX plots of (a) bare rGO, (b) pristine Mn_3O_4, (c) MnsR1, (d) MnsR0.75, (e) MnsR0.50, and (f) MnsR0.25.

be between 15 and 25 nm. Raman spectroscopy being an important tool is used in exploring the structural properties of the materials. The sharp peak at 651 cm^{-1} depicted in Figure 2 indicates the presence of Mn_3O_4 [42]. The Raman spectra of the reduced graphene oxide is depicted in Figure 2 with the characteristic peaks at 1359 and 1608 cm^{-1} corresponding to the D and G bands of reduced graphene oxide. The G band corresponds to the radial C-C stretching of the sp^2 carbon, and the D band relates to the first-order zone boundary phonon related to the defects on the edges of graphene. The intensity ratio (I_D/I_G) of the D and G bands was used to qualitatively characterize the defect density of rGO to be 0.8451 and 0.8576 for the composite MnsR1 [43].

The obtained crystallite size is nearly the same when compared to those obtained from the HR-SEM images. Mn_3O_4 exhibits a spherical morphology while rGO demonstrated a sheet-like morphology (Figures 3(a) and 3(b)), but in an agglomerated form which is attributed to the higher adsorption of moisture from the atmosphere. Mn_3O_4 nanospheres are clearly visualized in Figure 3(a) where the nanospheres are almost in the range of 15-29 nm. Figures 3(c)–3(f) demonstrate the even coating of Mn_3O_4 onto the rGO sheets. The EDAX spectrum of the samples also describes the quantitative analysis of the as-prepared samples. Figures 4(a)–4(f) illustrate the EDAX spectrum of rGO, Mn_3O_4, and the composites. The molecular structure of the synthesized samples was studied by FT-IR spectra (Figure 5). In the range 500-4000 cm^{-1} for rGO, the broad bands observed at 3338 cm^{-1} correspond to the strong stretching mode of the OH group [44], the absorption peak at 1635 cm^{-1} corresponds to the C=C stretching mode, and the peaks at 1716, 1154, and 1033 cm^{-1} correspond to the stretching modes of C=O, C–OH, and C–O, respectively.

FT-IR spectra of the Mn_3O_4 nanoparticles with absorption peaks at 620.10 cm^{-1} and 540.09 cm^{-1} correspond to the stretching vibration of Mn–O and Mn–O–Mn bonds indicating the formation of Mn_3O_4; the peak at 1636 cm^{-1} correspond to O-H bending vibrations. Figure 5 illustrates the molecular vibrational spectra for the rGO-composed Mn_3O_4 particles. The resulting vibrations at the lower frequency region suggested the formation of the Mn_3O_4 molecular structure. The vibrations at 3462 cm^{-1} may be assigned to the O-H stretching of adsorbed water, and the absorption bands at 1112 cm^{-1} are due to the molecular vibrations of C-O. The molecular vibrational band at 1636 cm^{-1} can be related to the O-H bending and C-O stretching vibrations. Thermogravimetric analysis was conducted to understand the thermal stability of MnsR1 nanocomposites. The experiments were performed up to 800°C in a nitrogen atmosphere at a heating rate of 10°C/min. Figure 6(a) depicts the TGA of the as-prepared rGO which indicates a significant weight loss linearly until it reaches around 450°C, attributed to the higher thermal stability of the sample followed by a sudden weight loss up to 600°C. Further, Figure 6(b) illustrates the TGA of Mn_3O_4; the TG depicts clearly three different regions of weight loss. Region 1 weight loss took place from room temperature to 300°C; this weight loss has been attributed to the removal of water from the specimen, namely, physisorbed molecular water and structural water, i.e., water of crystallization and chemically bound water. Region 2 in the range 390-610°C is attributed to the reduction of Mn from the specimen, and Region 3 from 650 to 800°C is attributed to the final decomposition of the specimen. Mn has higher thermal stability in comparison to other electrocatalysts. The composite MnsR1 has a lower total mass loss (about 15 wt%) than that of rGO (Figure 6(c)). The mass loss from 200 to 400°C can be attributed to the decomposition of rGO. Since Mn_3O_4 can withstand higher temperatures (about 500°C), the composite of MnsR1 only shows a gradual mass loss when the temperature is over 500°C. The difference in the total mass loss between rGO and MnsR1 is about 15 wt%. If it is assumed that Mn_3O_4 is thermally stable and does not have a mass loss below 600°C, the amount of Mn_3O_4 loaded in the MnsR1 is about 52.0 wt%.

3.1. Photocatalytic Performance. The photocatalytic performance of the prepared samples was carried out in the presence of visible light. The stock solution was prepared by dissolving 20 mg/l of phenol in distilled water and further taken for the analysis. 50 ml of the stock solution was placed in a dark room setup in order to block the interference of any stray light. The solution was placed on a stirrer, and 30 mg of the catalyst was added and left for 30 minutes in the dark to attain the adsorption desorption isotherm; after the collection of the sample, visible light via a 20 W bulb was introduced into the dark room for 15 minutes, and again, the sample was collected. The procedure was repeated until the completion of 120 minutes. The remaining sample was withdrawn via centrifugation after every cycle in order to carry out the repetition cycles. The degradation percentage was calculated as follows:

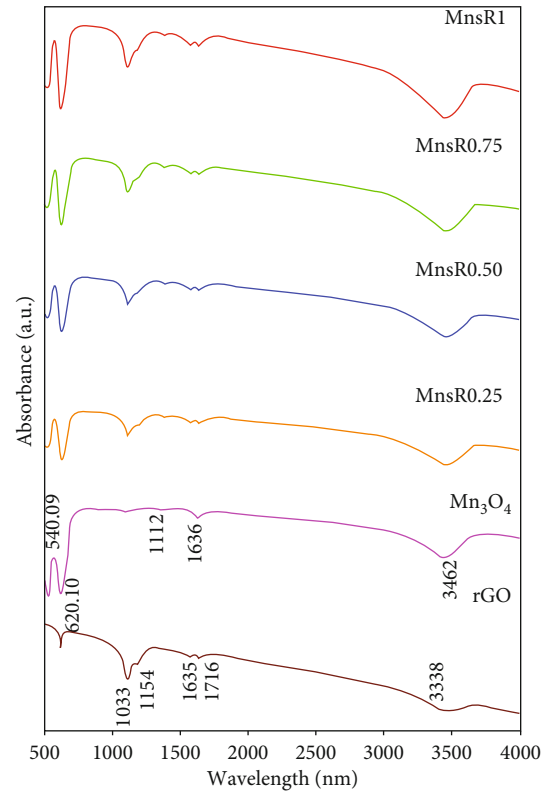

Figure 5: FT-IR spectra of bare rGO, pristine Mn_3O_4, MnsR0.25, MnsR0.50, MnsR0.75, and MnsR1.

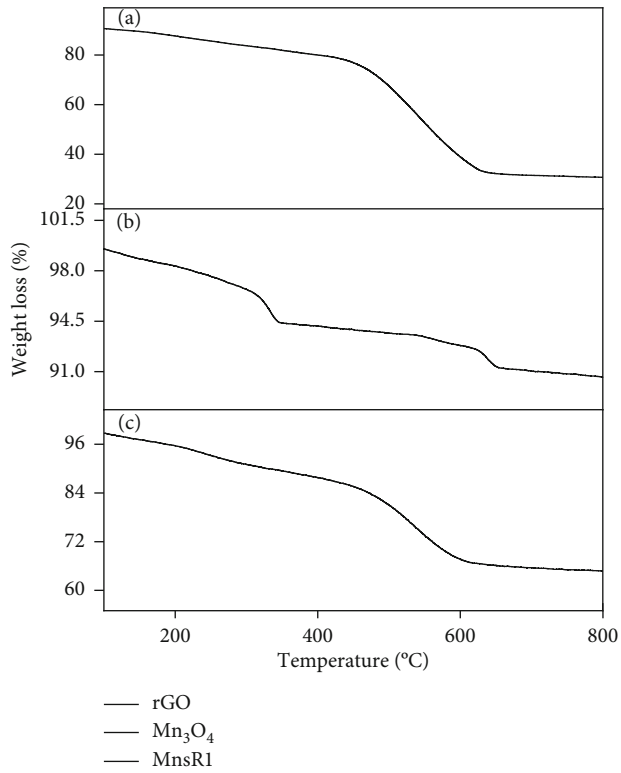

Figure 6: Thermogram of bare rGO, pristine Mn_3O_4, and MnsR1.

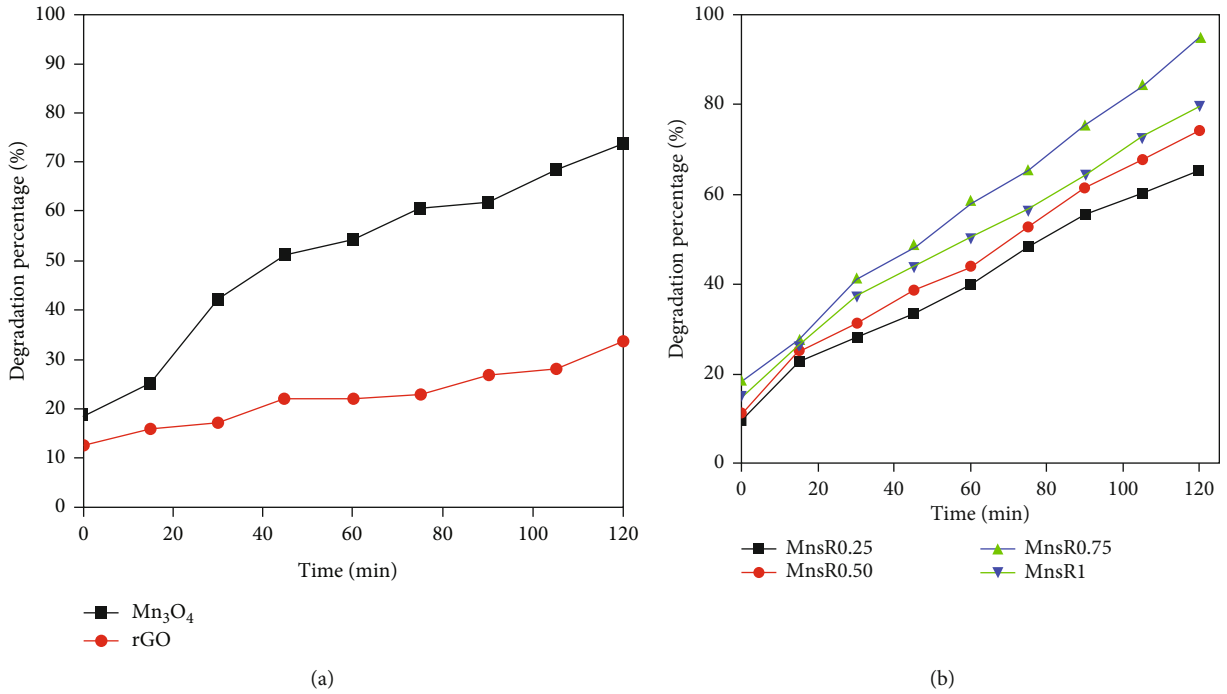

Figure 7: (a) Degradation percentage of rGO and pristine Mn_3O_4; (b) degradation percentage of MnsR0.25, MnsR0.50, MnsR0.75, and MnsR1.

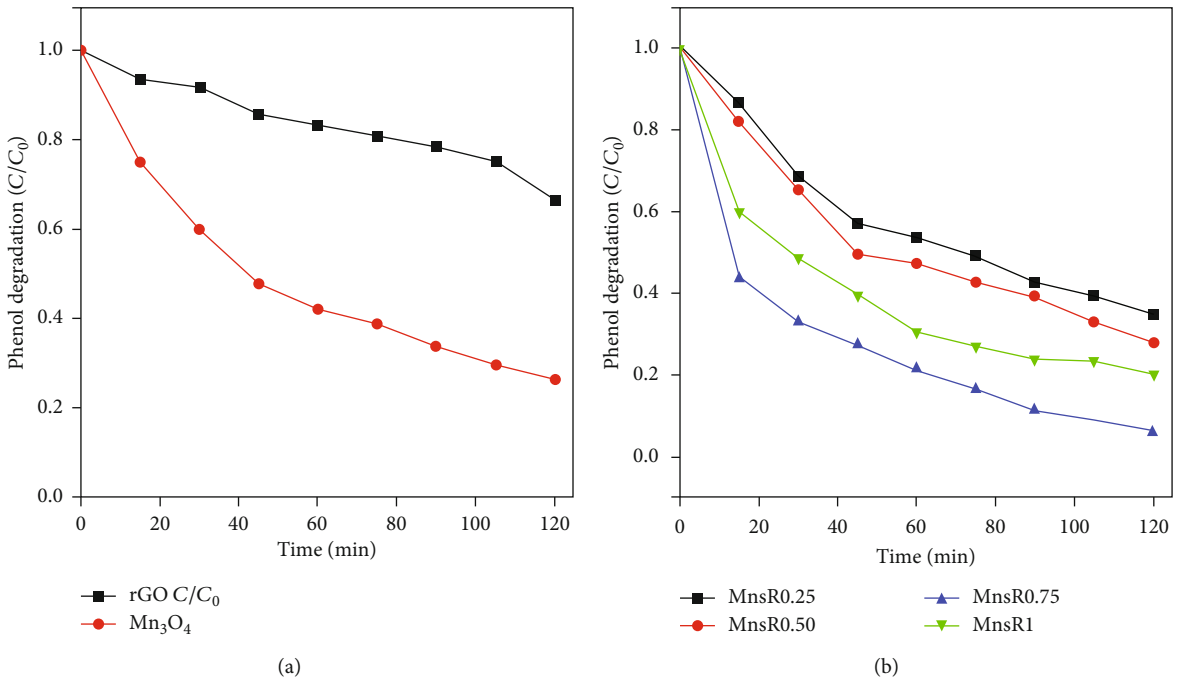

Figure 8: (a) Degradation concentration of rGO and pristine Mn_3O_4 and (b) absorbance percentage of MnsR0.25, MnsR0.50, MnsR0.75, and MnsR1.

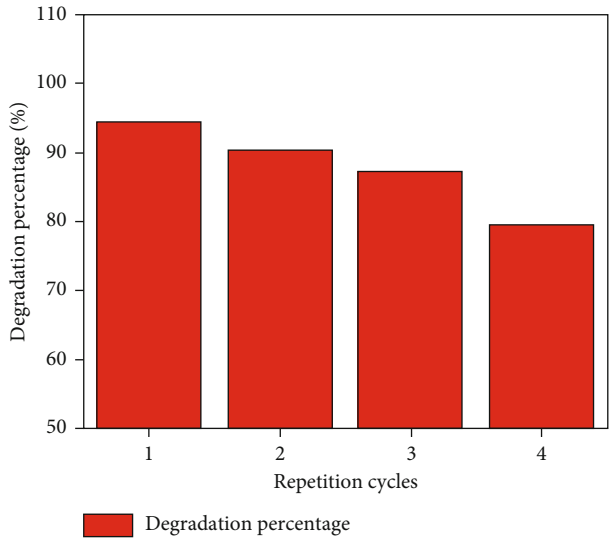

Figure 9: Repetition cycles of MnsR0.75.

$$\mathrm{DE} = 1 - \left(\frac{T}{T_0}\right) \times 100, \tag{2}$$

where DE is the degradation efficiency, T is the concentration of the analyte at time 0 minute, and T_0 is the concentration of the analyte at various time intervals. The photocatalytic performance of the prepared samples was evaluated by the photocatalytic decomposition of aqueous phenol solution under visible light irradiation. From Figure 7, it is evident that rGO exhibits a lower degradation activity than the metal oxide. On further studies at the 120^{th} minute, a total of 33.5% was achieved in the case of pure rGO.

On the other hand, pristine Mn_3O_4 exhibits a degradation of 18.6% at the zeroth minute, and as the time increases with irradiation of visible light, a net degradation of 73.6% was achieved. The composites exhibited an average degradation of 14% at the 0^{th} min, and maximum degradation of 94.48% was achieved for the MnsR0.75 sample (Figures 7(a) and 7(b)).

On further increasing the concentration of Mn_3O_4, it is evident that the degradation percentage decreasing this could be attributed to the agglomeration occurring between the rGO sheets. The $\pi - \pi$ stacking interaction provides a greater amount of phenol concentration near the Mn_3O_4 nanoparticles on the surface of rGO and therefore leads to the more efficient contact between them. Due to its excellent electric conductivity and large specific surface area, it acts as an efficient electron acceptor to enhance the photoinduced charge transfer mechanism. This condition is also hindered in cases when the rGO concentration goes higher as in the MnsR1 composite. Figures 8(a) and 8(b) display the reduction ratio with respect to time. From the degradation percentage, it is evident that the sample MnsR0.75 exhibited the highest degradation, repetition of the experiment was carried out, and the sample was found to degrade around 90%, 87%, and 79% in the repetition cycle as depicted in Figure 9. On further repetition, it was found to decrease to around 52%.

4. Conclusion

In conclusion, Mn_3O_4 nanoparticles were loaded onto the graphene surface by a simple thermal route. Solvent-ethylene glycol played a vital role in the formation of the as-prepared product. The small-sized Mn_3O_4 nanoparticles and high surface area of the reduced graphene oxide composite exhibited better catalytic activity under visible light irradiation. The photocatalyst is highly stable and has been used for four successive times without any significant loss in its activity. The nanocomposite MnsR0.75 exhibited the highest phenol degradation of 94.48%, taking into account the presence of rGO in (i) the utilization of a higher number of photoelectrons and (ii) lowering of electron hole recombination. The high activity exhibited was ascribed due to the strong interaction and progress of synergetic effect between the Mn_3O_4 nanospheres and rGO. Thus, the MnsRnanocomposites can be considered a promising material for the removal of various harmful organic dyes from wastewater.

Data Availability

The data supporting this work is available from the corresponding author upon request.

Conflicts of Interest

The authors declare that they have no conflicts of interest.

References

[1] L. F. Liotta, M. Gruttadauria, G. Di Carlo, G. Perrini, and V. Librando, "Heterogeneous catalytic degradation of phenolic substrates: catalysts activity," *Journal of Hazardous Materials*, vol. 162, no. 2-3, pp. 588–606, 2009.

[2] E. M. Seftel, M. Niarchos, C. Mitropoulos, M. Mertens, E. F. Vansant, and P. Cool, "Photocatalytic removal of phenol and methylene-blue in aqueous media using TiO_2@LDH clay nanocomposites," *Catalysis Today*, vol. 252, pp. 120–127, 2015.

[3] C. Su, X. Duan, J. Miao et al., "Mixed conducting perovskite materials as superior catalysts for fast aqueous-phase advanced oxidation: a mechanistic study," *ACS Catalysis*, vol. 7, no. 1, pp. 388–397, 2017.

[4] L. J. Alemany and M. A. Ban, "Photodegradation of phenol in water using silica-supported titania catalysts," *Applied Catalysis B: Environmental*, vol. 13, no. 3-4, pp. 289–297, 1997.

[5] Y. Liu, L. Yu, C. N. Ong, and J. Xie, "Nitrogen-doped graphene nanosheets as reactive water purification membranes," *Nano Research*, vol. 9, no. 7, pp. 1983–1993, 2016.

[6] R. Kumar, S. Sahoo, E. Joanni et al., "Heteroatom doped graphene engineering for energy storage and conversion," *Materials Today*, vol. 39, pp. 47–65, 2020.

[7] N. Calace, E. Nardi, B. M. Petronio, and M. Pietroletti, "Adsorption of phenols by papermill sludges," *Environmental Pollution*, vol. 118, no. 3, pp. 315–319, 2002.

[8] N. S. Inchaurrondo, P. Massa, R. Fenoglio, J. Font, and P. Haure, "Efficient catalytic wet peroxide oxidation of phenol at moderate temperature using a high-load supported copper catalyst," *Chemical Engineering Journal*, vol. 198-199, pp. 426–434, 2012.

[9] M. Asadollahi-Baboli, "Exploring QSTR analysis of the toxicity of phenols and thiophenols using machine learning methods," *Environmental Toxicology and Pharmacology*, vol. 34, no. 3, pp. 826–831, 2012.

[10] R. Gopal, M. M. Chinnapan, A. K. Bojarajan et al., "Facile synthesis and defect optimization of 2D-layered MoS_2 on TiO_2 heterostructure for industrial effluent, wastewater treatments," *Scientific Reports*, vol. 10, no. 1, p. 21625, 2020.

[11] A. Mohamed, T. A. Osman, M. S. Toprak, M. Muhammed, and A. Uheida, "Surface functionalized composite nanofibers for efficient removal of arsenic from aqueous solutions," *Chemosphere*, vol. 180, pp. 108–116, 2017.

[12] R. Kumar, R. Matsuo, K. Kishida, M. M. Abdel-Galeil, Y. Suda, and A. Matsuda, "Homogeneous reduced graphene oxide supported NiO-MnO_2 ternary hybrids for electrode material with improved capacitive performance," *Electrochimica Acta*, vol. 303, pp. 246–256, 2019.

[13] A. Mohamed, R. El-Sayed, T. A. Osman, M. S. Toprak, M. Muhammed, and A. Uheida, "Composite nanofibers for highly efficient photocatalytic degradation of organic dyes from contaminated water," *Environmental Research*, vol. 145, pp. 18–25, 2016.

[14] F. Zhang, M. Li, W. Li et al., "Degradation of phenol by a combined independent photocatalytic and electrochemical process," *Chemical Engineering Journal*, vol. 175, pp. 349–355, 2011.

[15] D. P. Zagklis, A. I. Vavouraki, M. E. Kornaros, and C. A. Paraskeva, "Purification of olive mill wastewater phenols through membrane filtration and resin adsorption/desorption," *Journal of Hazardous Materials*, vol. 285, pp. 69–76, 2015.

[16] L. D. Naidu, S. Saravanan, M. Goel, S. Periasamy, and P. Stroeve, "A novel technique for detoxification of phenol from wastewater: nanoparticle assisted nano filtration (NANF)," *Iranian Journal of Environmental Health Science & Engineering*, vol. 14, no. 1, p. 9, 2016.

[17] S. Wang, D. Shi, R. Yang, Y. Xu, H. Guo, and X. Yang, "Solvent extraction of phenol from aqueous solution with benzyl 2-ethylhexyl sulfoxide as a novel extractant," *Canadian Journal of Chemical Engineering*, vol. 93, no. 10, pp. 1787–1792, 2015.

[18] N. L. Zabik, C. N. Virca, T. M. McCormick, and S. Martic-Milne, "Selective electrochemical versus chemical oxidation of bulky phenol," *The Journal of Physical Chemistry. B*, vol. 120, no. 34, pp. 8914–8924, 2016.

[19] C. M. Magdalane, K. Kaviyarasu, M. V. Arularasu, K. Kanimozhi, and G. Ramalingam, "Structural and morphological properties of Co_3O_4 nanostructures: investigation of low temperature oxidation for photocatalytic application for waste water treatment," *Surfaces and Interfaces*, vol. 17, p. 100369, 2019.

[20] B. Palanivel, M. Lallimathi, B. Arjunkumar et al., "rGO supported g-C_3N_4/$CoFe_2O_4$ heterojunction: Visible-light-active photocatalyst for effective utilization of H_2O_2 to organic pollutant degradation and $OH^{\bullet}$ radicals production," *Journal of Environmental Chemical Engineering*, vol. 9, no. 1, p. 104698, 2021.

[21] G. Ramalingam, J. Madhavan, P. Sagayaraj, S. Selvakumar, R. Gunaseelan, and R. Jerald Vijay, "Synthesis and characterization of one dimensional semiconducting nanorods and nanobelts," *Transactions of the Indian Institute of Metals*, vol. 64, no. 1-2, pp. 217–220, 2011.

[22] Y. Wang, Y. Xie, H. Sun, J. Xiao, H. Cao, and S. Wang, "2D/2D nano-hybrids of γ-MnO_2 on reduced graphene oxide for catalytic ozonation and coupling peroxymonosulfate activation," *Journal of Hazardous Materials*, vol. 301, pp. 56–64, 2016.

[23] M. Ramesh, M. P. Rao, F. Rossignol, and H. S. Nagaraja, "rGO/MnO2 nanowires for ultrasonic-combined Fenton assisted efficient degradation of reactive black 5," *Water Science and Technology*, vol. 76, no. 7, pp. 1652–1665, 2017.

[24] J. Qu, L. Shi, C. He et al., "Highly efficient synthesis of graphene/MnO_2 hybrids and their application for ultrafast oxidative decomposition of methylene blue," *New York*, vol. 66, pp. 485–492, 2014.

[25] J. Xu, W. Wang, M. Shang, E. Gao, Z. Zhang, and J. Ren, "Electrospun nanofibers of bi-doped TiO_2 with high photocatalytic activity under visible light irradiation," *Journal of Hazardous Materials*, vol. 196, pp. 426–430, 2011.

[26] E. Saputra, S. Muhammad, H. Sun, H.-M. Ang, M. O. Tadé, and S. Wang, "Manganese oxides at different oxidation states for heterogeneous activation of peroxymonosulfate for phenol degradation in aqueous solutions," *Applied Catalysis B: Environmental*, vol. 142-143, pp. 729–735, 2013.

[27] J. C. Contreras-Ruiz, S. Martínez-Gallegos, E. Ordoñez, J. C. González-Juárez, and J. L. García-Rivas, "Synthesis of hydroxide–TiO2 compounds with photocatalytic activity for degradation of phenol," *Journal of Electronic Materials*, vol. 46, no. 3, pp. 1658–1668, 2017.

[28] A. Salama, A. Mohamed, N. M. Aboamera, T. A. Osman, and A. Khattab, "Photocatalytic degradation of organic dyes using composite nanofibers under UV irradiation," *Applied Nanoscience*, vol. 8, no. 1-2, pp. 155–161, 2018.

[29] M. G. Yazdi, M. Ivanic, A. Mohamed, and A. Uheida, "Surface modified composite nanofibers for the removal of indigo carmine dye from polluted water," *RSC Advances*, vol. 8, no. 43, pp. 24588–24598, 2018.

[30] X. Duan, C. Su, L. Zhou et al., "Surface controlled generation of reactive radicals from persulfate by carbocatalysis on nanodiamonds," *Applied Catalysis B: Environmental*, vol. 194, pp. 7–15, 2016.

[31] J. Kang, X. Duan, L. Zhou, H. Sun, M. O. Tadé, and S. Wang, "Carbocatalytic activation of persulfate for removal of antibiotics in water solutions," *Chemical Engineering Journal*, vol. 288, pp. 399–405, 2016.

[32] A. H. Mady, M. L. Baynosa, D. Tuma, and J.-J. Shim, "Facile microwave-assisted green synthesis of Ag- $ZnFe_2O_4$@rGO nanocomposites for efficient removal of organic dyes under UV- and visible-light irradiation," *Applied Catalysis B: Environmental*, vol. 203, pp. 416–427, 2017.

[33] M. M. Kadam, K. B. Dhopte, N. Jha, V. G. Gaikar, and P. R. Nemade, "Synthesis, characterization and application of γ-MnO2/graphene oxide for the selective aerobic oxidation of benzyl alcohols to corresponding carbonyl compounds," *New Journal of Chemistry*, vol. 40, no. 2, pp. 1436–1442, 2016.

[34] T. Zeng, X. Zhang, S. Wang, H. Niu, and Y. Cai, "Spatial confinement of a Co_3O_4 catalyst in hollow metal–organic frameworks as a nanoreactor for improved degradation of organic pollutants," *Environmental Science & Technology*, vol. 49, no. 4, pp. 2350–2357, 2015.

[35] S. Zhang, Q. Fan, H. Gao et al., "Formation of Fe_3O_4@MnO_2 ball-in-ball hollow spheres as a high performance catalyst with enhanced catalytic performances," *Journal of Materials Chemistry A*, vol. 4, no. 4, pp. 1414–1422, 2016.

[36] P. Húmpola, H. Odetti, J. C. Moreno-Piraján, and L. Giraldo, "Activated carbons obtained from agro-industrial waste:

textural analysis and adsorption environmental pollutants," *Adsorption*, vol. 22, no. 1, pp. 23–31, 2016.

[37] J. Zhang, X. Li, H. Chen et al., "Hydrogen production by catalytic methane decomposition: carbon materials as catalysts or catalyst supports," *International Journal of Hydrogen Energy*, vol. 42, no. 31, pp. 19755–19775, 2017.

[38] I. Velo-Gala, J. J. López-Peñalver, M. Sánchez-Polo, and J. Rivera-Utrilla, "Role of activated carbon surface chemistry in its photocatalytic activity and the generation of oxidant radicals under UV or solar radiation," *Applied Catalysis B: Environmental*, vol. 207, pp. 412–423, 2017.

[39] T. Sivakumar Natarajan, H. C. Bajaj, and R. J. Tayade, "Palmyra tuber peel derived activated carbon and anatase TiO_2 nanotube based nanocomposites with enhanced photocatalytic performance in rhodamine 6G dye degradation," *Process Safety and Environment Protection*, vol. 104, pp. 346–357, 2016.

[40] B. Boucher, R. Buhl, and M. Perrin, "Proprietes et structure magnetique de Mn_3O_4," *Journal of Physics and Chemistry of Solids*, vol. 32, no. 10, pp. 2429–2437, 1971.

[41] Y. Cao, X. Lin, C. Zhang et al., "MnO2nanoflakes anchored on reduced graphene oxide nanosheets as high performance anode materials for lithium-ion batteries," *RSC Advances*, vol. 4, no. 57, pp. 30150–30155, 2014.

[42] H. Gao, F. Xiao, C. B. Ching, and H. Duan, "Flexible all-solid-state asymmetric supercapacitors based on free-standing carbon nanotube/graphene and Mn3O4 nanoparticle/graphene paper electrodes," *ACS Applied Materials & Interfaces*, vol. 4, no. 12, pp. 7020–7026, 2012.

[43] H.-L. Guo, X.-F. Wang, Q.-Y. Qian, F.-B. Wang, and X.-H. Xia, "A green approach to the synthesis of graphene nanosheets," *ACS Nano*, vol. 3, no. 9, pp. 2653–2659, 2009.

[44] N. Zhang, C. Fu, D. Liu, Y. Li, H. Zhou, and Y. Kuang, "Three-Dimensional Pompon-like MnO_2/Graphene Hydrogel Composite for Supercapacitor," *Electrochimica Acta*, vol. 210, pp. 804–811, 2016.